FIRST STREET FOUNDATION

First Street Foundation Flood Model (FSF-FM)

Technical Methodology Documentation

Version 3.0

Published: 7/31/2023

Acknowledgements

We would like to thank all collaborators and partners for their support in developing this new version of the First Street Foundation Flood Model (FSF-FM). Thank you to the Rhodium Group, a modeling partner dedicated to producing downscaled, bias-corrected climate projection data and tropical cyclone-driven surge data, accounting for current and future climate change, including extreme events. We give a special thank you to our board member, Dr. Kerry Emanuel at Massachusetts Institute of Technology, for his contributions and feedback. In this version, he was supportive of the First Street Foundation Precipitation Model (FSF-PM) development, which is the primary achievement of this version. Also, we appreciate all board members and individuals at First Street Foundation who provided time and effort unsparingly.

FIRST STREET FOUNDATION

Table of Contents

Abbreviations

American Society of Adaptation Professionals (ASAP)

Annual Exceedance Probability (AEP)

Annual Maximum Precipitation (AMP)

Annual Maximum Series (AMS)

Automated Surface Observing System (ASOS)

Conterminous United States (CONUS)

Coupled Model Intercomparison Project Phase 6 (CMIP6)

Digital Elevation Model (DEM)

Extreme Science and Engineering Discovery Environment (XSEDE)

Federal Emergency Management Agency (FEMA)

FEMA Flood Insurance Studies (FIS)

First Street Foundation (FSF)

First Street Foundation Flood Model (FSF-FM)

First Street Foundation Precipitation Model (FSF-PM)

Fluvial Change Factor (FCF)

General Circulation Model (GCM)

Global Downscaled Projections for Climate Impacts Research (GDPCIR)

Global Runoff Data Centre (GRDC)

Global Tide and Surge Model (GTSM)

Hydrologiska Byråns Vattenbalansavdelning (HBV)

Intensity-Duration-Frequency (IDF)

Intergovernmental Panel on Climate Change (IPCC)

International Best Track Archive for Climate Stewardship (IBTrACS)

National Centers for Environmental Prediction (NCEP)

National Elevation Dataset (NED)

National Hurricane Center (NHC)

National Hydrography Dataset (NHDPlus)

National Inventory of Dams (NID)

National Land Cover Dataset (NLCD)

National Oceanic and Atmospheric Administration (NOAA)

National Science Foundation (NSF)

NOAA's Vertical Datum Transformation (VDatum)
North American Mesoscale Forecast System (NAM)
North American Vertical Datum (NAVD 88)
Parameter-elevation Regressions on Independent Slopes Model (PRISM)
Pluvial Change Factor (PCF)
Precipitation Frequency Estimate (PFE)
Regional Frequency Analysis (RFA)
Regionalized Flood Frequency Analysis (RFFA)
Shared Socioeconomic Pathways (SSP)
Sixth Assessment Report (AR6)
United States Geological Survey (USGS)
US Army Corps of Engineers (USACE)
USACE National Levee Database (NLD)
USDA Gridded Soil Survey Geographic Database (gSSURGO)
USGS Hydrologic Unit Code (HUC)
WAVEWATCH III (WWW3)

1. Executive Summary

First Street Foundation (FSF), in partnership with the Rhodium Group and Dr. Emanuel's research group at Massachusetts Institute of Technology, has collaborated to develop the new third version (V3) of the First Street Foundation Flood Model (FSF-FM) in 2023. This new version of the FSF-FM has been created with the focused purpose of assessing flood risk at the individual property level, under changes in climate and extreme weather in the United States. This document aims to address the technical background of data sources, methodologies, and implementation processes FSF employed to develop the new version of the FSF-FM.

In this new version, the FSF-FM exceeds the benefits of the previous versions by including a newly developed precipitation model and the latest climate projection data. The primary feature of this version is the development of the First Street Foundation Precipitation Model (FSF-PM). The FSF-PM is the precipitation frequency estimation model to produce climate-adjusted precipitation for a specific scenario (e.g., a 1-in-100-year precipitation depth in 2023 or 2053). This model is developed based on understanding the well-known limitations in the NOAA Atlas 14, diverging from the recent 20-year records due to precipitation non-stationarity across the United States (Kim et al., 2022; 2023). According to the FSF-PM, we confirmed that the majority of the United States faces three times more occurrences of extreme storms corresponding to a 1-in-100-year return period of the 20th century, suggesting that the recent 20-year extreme events should be treated as the "new normal". This update helps the FSF-FM identify new pluvial flooding-prone areas according to changes in extreme precipitation in the 21st century.

The second feature is the inclusion of the updated climate projection data, Coupled Model Intercomparison Project Phase 6 (CMIP6) and Intergovernmental Panel on Climate Change (IPCC) Sixth Assessment Report (AR6). The climate data plays an important role in providing future changes in the hydrological cycle and meteorological factors, such as precipitation and temperature in the FSF-FM. CMIP6 was used to develop new climate adjustment factors, scaling the historical flood risk according to changes in extreme precipitation properties and hydrological responses in the future. Sea level change projections from AR6 and storm surges from and tropical cyclone modeling are mainly considered to estimate physical flood risk in the East, Gulf, and West Coasts of the United States.

This document is organized transparently around our model development methods in order to give users a clear understanding of 1) how the model was developed, 2) the strengths and weaknesses of the model, and 3) any potential limitations associated with the techniques and decisions made in the creation of the models. This documentation is organized as follows: Section ‘First Street Foundation Flood Model’ introduces the flood modeling framework and associated key drivers in flood modeling. Sections ‘Pluvial Flood Risk Modeling’, ‘Fluvial Flood Risk Modeling’, and ‘Coastal Flood Risk Modeling’ present the updated components based on new data and methods, which are the core features of this new version. Section ‘Hazard Layer’ describes practical modeling processes with the developed model input components and post-processing methods for finalizing high-resolution flood inundation maps at a national scale.

2. First Street Foundation Flood Model

2.1 Framework

The FSF-FM consists of four major components, inland (e.g., pluvial and fluvial) flood modeling, coastal flood modeling, computing (flood model execution), and post-processing, for producing flood hazard layers. Fig. 1 shows the framework of the flood hazard layers (e.g, inundation water mask and depth) development built upon the FSF-FM from data collection to post-processing.

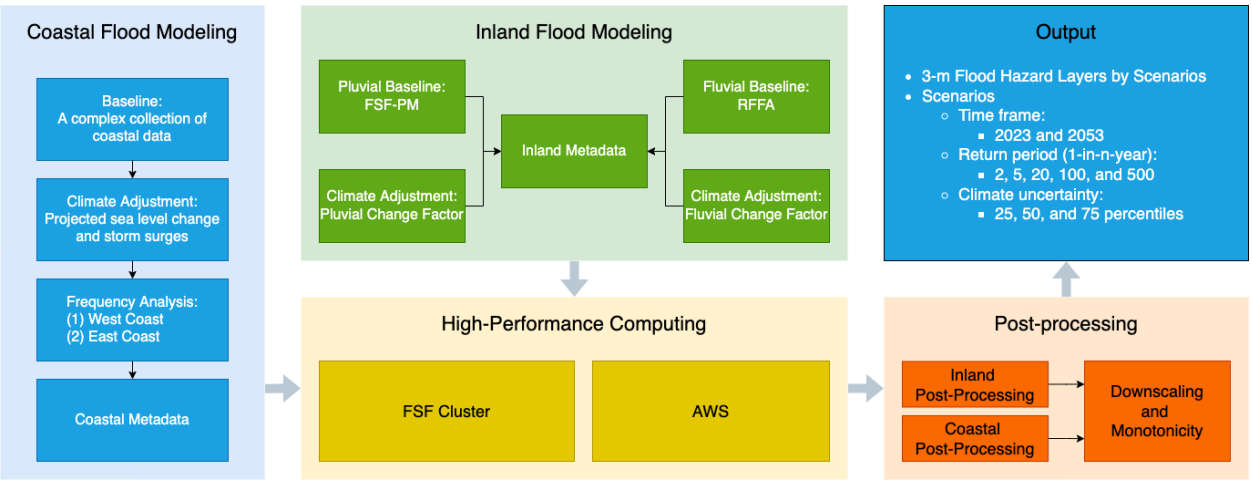

Figure 1. A workflow chart of the flood model development

In the FSF-FM, the inland flood modeling is responsible for accounting for precipitation-driven ('Pluvial') and riverine ('Fluvial') flood risk. Pluvial modeling aims to simulate flood water depths in small watersheds (drainage area < 50 km^2), where heavy precipitation is the dominant source of flooding. Fluvial modeling aims to simulate flooding when streams and rivers exceed the capacity of their natural or constructed channels to accommodate water flow and water overflows the banks, spilling out into adjacent low-lying, dry land. The main river channels and tributaries are the target for simulating flood water depths by overflows.

In inland flood modeling, each component has two sub-components called 'Baseline' and 'Climate Adjustment.' The baseline is a standard to represent the historical properties of each flooding source, such as precipitation depth and streamflow rate. It forms an intensity-frequency or

intensity-duration-frequency curve derived from the regional frequency analysis and observed records, and it provides a value corresponding to a specific return period (i.e., recurrence interval). Climate adjustment is the process of projecting future risk by scaling the baseline with climate change factors. In this process, the climate change factors, pluvial and fluvial change factors, are the core estimate allowing to reflect climate change-driven effects on changes in precipitation and streamflow in the flood modeling. Both the baseline and climate change factors are archived in the metadata, and they are utilized in creating inputs for running the FSF-FM.

The processes in the coastal flood modeling generate climate-adjusted water surface elevations along the West, East, and Gulf Coasts. For the West Coast, this involves merging water levels and tides with projected sea level rise based on CMIP 6 outputs. The East and Gulf Coasts share the same concept, but it is more complex due to hurricane activity in the Atlantic Ocean and Gulf of Mexico. Therefore, projected hurricane storm surge depths must also be added to the levels, tides, and sea level rise. More specifically, the coastal pre-processing objective is to create coastal boundary files that contain normalized time series and exceedance probability scaled return period curves at every coastal boundary location. This information is required for every desired year, quantile, and return period combination modeled.

Three flooding sources are separately simulated in the FSF-FM and merged to account for the combined flood risk. For computation efficiency, the U.S. domain is tiled by a 1.5 x 1.5-degree tile with a 0.25-degree overlapped portion and simulated for a set of scenarios (e.g., durations, return periods, climate scenarios, etc). Thirty meter resolution inundation maps from the FSF-FM are post-processed and downscaled to a 3-meter resolution, which is a fine high resolution to represent a flood risk at a property level. As part of the data quality control process, a monotonicity process is implemented to identify discrepancies of simulated water depth across the scenarios and correct them by considering a relationship between the upper and lower scenarios' expectations. The FSF-FM produces flood inundation maps as hazard layers for various scenario components such as different time frames (2023 and 2053), return periods (5, 20, 100, and 500-year), and climate uncertainty levels (25, 50, and 75 percentiles of climate projection ensembles).

2.2 Climate Change

2.2.1 Coupled Model Intercomparison Phase 6 (CMIP6)

The World Climate Research Programme's 6th Coupled Model Intercomparison Project (CMIP6) is employed for the climate adjustments in the development of the FSF-FM V3. CMIP6 is an enormous advancement in the quality, detail, and scope of climate modeling. The Global Downscaled Projections for Climate Impacts Research (GDPCIR) dataset makes this modeling more applicable to understanding the impacts of changes in the climate on humans and society with two key developments: trend-preserving bias correction and downscaling.

GDPCIR provides global, daily minimum and maximum air temperature at the surface (tasmin and tasmax) and daily cumulative surface precipitation (pr) corresponding to the CMIP6 historical SSP1-2.6, SSP2-4.5, SSP3-7.0, and SSP5-8.5 scenarios for 25 global climate models on a 1/4-degree regular global grid. This dataset is built upon Quantile Delta Mapping (Cannon et al 2015) for the bias correction algorithm, which reasonably corrects the full distribution to observations and preserves quantile-specific trends by calendar month rather than shifting the distribution using the mean General Circulation Model (GCM) trend over a given location as in the bias correction and spatial downscaling (BCSD). GDPCIR used in the FSF-FM development is available from the Microsoft Planetary Computer (https://planetarycomputer.microsoft.com/dataset/group/cil-gdpcir).

Among the given scenarios in the CMIP6, the SSP2-4.5 scenario, which is considered as the most realistic scenario under the current climate conditions and changing climate state, is used to produce the FSF-FM modeling components such as climate adjustment factors (i.e., pluvial and fluvial change factors) and coastal surge simulation. Table 1 shows the list of GCMs used in the FSF-FM development. The 18 GCMs which provide the SSP2-4.5 scenario are primarily selected. In this development, all GCMs listed in the table were utilized.

Table 1 Features of CMIP6 GCM models used in the version 3

Modeling institution	Source Model	Available experiments	License collection
CAS	FGOALS-g3	SSP2-4.5, SSP3-7.0, SSP5-8.5	Public domain datasets
INM	INM-CM4-8	SSP1-2.6, SSP2-4.5, SSP3-7.0, SSP5-8.5	Public domain datasets
INM	INM-CM5-0	SSP1-2.6, SSP2-4.5, SSP3-7.0, SSP5-8.5	Public domain datasets
BCC	BCC-CSM2-MR	SSP1-2.6, SSP2-4.5, SSP3-7.0, SSP5-8.5	CC-BY-40
CMCC	CMCC-CM2-SR5	SSP1-2.6, SSP2-4.5, SSP3-7.0, SSP5-8.5	CC-BY-40
CMCC	CMCC-ESM2	SSP1-2.6, SSP2-4.5, SSP3-7.0, SSP5-8.5	CC-BY-40
CSIRO-ARCCSS	ACCESS-CM2	SSP2-4.5, SSP3-7.0	CC-BY-40
CSIRO	ACCESS-ESM1-5	SSP1-2.6, SSP2-4.5, SSP3-7.0	CC-BY-40
MIROC	MIROC-ES2L	SSP1-2.6, SSP2-4.5, SSP3-7.0, SSP5-8.5	CC-BY-40
MIROC	MIROC6	SSP1-2.6, SSP2-4.5, SSP3-7.0, SSP5-8.5	CC-BY-40
MOHC	UKESM1-0-LL	SSP1-2.6, SSP2-4.5, SSP3-7.0, SSP5-8.5	CC-BY-40
MPI-M	MPI-ESM1-2-LR	SSP1-2.6, SSP2-4.5, SSP3-7.0, SSP5-8.5	CC-BY-40
NCC	NorESM2-LM	SSP1-2.6, SSP5-8.5	CC-BY-40
NCC	NorESM2-MM	SSP1-2.6, SSP2-4.5, SSP3-7.0, SSP5-8.5	CC-BY-40
NOAA-GFDL	GFDL-ESM4	SSP1-2.6, SSP5-8.5	CC-BY-40
EC-Earth-Consortium	EC-Earth3	SSP1-2.6, SSP2-4.5, SSP3-7.0, SSP5-8.5	CC-BY-40
EC-Earth-Consorti	EC-Earth3-Veg	SSP1-2.6, SSP2-4.5, SSP3-7.0,	CC-BY-40

um		SSP5-8.5	
EC-Earth-Consortium	EC-Earth3-Veg-LR	SSP1-2.6, SSP2-4.5, SSP3-7.0, SSP5-8.5	CC-BY-40

Historical data is daily, excluding leap days, from Jan 1, 1950 to Dec 31, 2014; SSP data is daily, excluding leap days, from Jan 1, 2015 to either Dec 31, 2099 or Dec 31, 2100, depending on data availability in the source GCM. The spatial domain covers all 0.25-degree grid cells, indexed by the grid center, with grid edges on the quarter-degree, using a -180 to 180 longitude convention. Thus, the "lon" coordinate extends from -179.875 to 179.875, and the "lat" coordinate extends from -89.875 to 89.875, with intermediate values at each 0.25-degree increment between (e.g. -179.875, -179.625, -179.375, etc).

2.2.2 IPCC Sixth Assessment Report (AR6)

To capture current and future sea level projections along the coasts, the IPCC AR6 Sea Level Change Projections (zenodo.org/record/6382554) used in V3 originated from the Working Group I contribution to the IPCC AR6, released on 9-Aug-2021 in Chapter 9: Ocean, Cryosphere and Sea Level Change (www.ipcc.ch/report/ar6/wg1/). CMIP6 outputs were used to produce these projections. The Interagency Task Force offers downscaled sea level projections created from AR6 (Sweet et al., 2022) in global and regional sea level rise scenarios for the United States (http://www.usgs.gov/publications/global-and-regional-sea-level-rise-scenarios-united-states), but the scenarios are based on targeted amounts of sea level rise. Instead, the AR6 projections' framing is based on the Shared Socioeconomic Pathways (SSP), which is consistent with the FSF-FM.

Specifically, the FSF-FM uses the regional medium confidence SSP245 values, total integrated over all components for 2020, 2030, 2040, 2050, and 2060, quantiles 0.167, 0.50, and 0.833. SSP370 values were considered for V3, but after careful analysis, they were found to be too similar to the SSP245 values. Since 2023 represents the current and 2053 represents the future in V3, the values were calculated using a linear trend function (Table 2). Additionally, the

Table 2. Sample of AR6 sea level projections converted to 2023 and 2053 using a linear trend function

Location	PSMSL ID	Lat	Lon	2020	2030	2023	2050	2060	2053
BOSTON, MA	235	42.3539	-71.0503	96	169	117.9	341	426	366.5
WOODS HOLE, MA	367	41.5236	-70.6711	101	177	123.8	356	444	382.4
NANTUCKET, MA	1111	41.2853	-70.0964	106	185	129.7	372	462	399
NEWPORT, RI	351	41.5044	-71.3261	99	173	121.2	350	436	375.8
PROVIDENCE, RI	430	41.8067	-71.4006	93	164	114.3	332	414	356.6
NEW LONDON, CT	429	41.355	-72.0867	98	173	120.5	348	434	373.8
BRIDGEPORT, CT	1068	41.1758	-73.184	97	170	118.9	342	425	366.9
MONTAUK, NY	519	41.0483	-71.9594	106	185	129.7	370	460	397

FSF-FM requires values referenced to the North American Vertical Datum (NAVD 88). Thus, these trended values were converted from millimeters to meters and vertically transformed to NAVD 88 using NOAA's Vertical Datum Transformation (VDatum) tool (vdatum.noaa.gov). Table 3 illustrates some of these transformations.

Table 3. AR6 sea level projections vertically transformed to NAVD 88

Location	PSMSL ID	Lat	Lon	2023 (mm)	2023 (m)	2023 NAVD 88 (m)
BOSTON, MA	235	42.3539	-71.0503	117.9	0.1179	0.02465
WOODS HOLE,	367	41.523	-70.67	123.8	0.1238	0.0087

MA		6	11			
NANTUCKET, MA	1111	41.2853	-70.0964	129.7	0.1297	0.04819
NEWPORT, RI	351	41.5044	-71.3261	121.2	0.1212	0.028
PROVIDENCE, RI	430	41.8067	-71.4006	114.3	0.1143	0.04608
NEW LONDON, CT	429	41.355	-72.0867	120.5	0.205	0.02797
BRIDGEPORT, CT	1068	41.1758	-73.184	118.9	0.1189	0.05225
MONTAUK, NY	519	41.0483	-71.9594	129.7	0.1297	0.02863

2.2.3 Tropical Cyclone: Synthetic Storm Simulation Data

The Rhodium Group partners with Dr. Kerry Emanuel, of the Massachusetts Institute of Technology and WindRiskTech LLC, for the tropical cyclone hazard portion of our climate model. With this partnership, we leverage decades of climate and tropical cyclone modeling development to capture projected changes in tropical cyclone activity. The methods driving the projected tropical cyclone tracks have been studied and documented extensively by Dr. Emanuel and his research partners (e.g., Emanuel et al., 2006; Knutson et al., 2020; WindRiskTech, n.d.). An overview of how we analyze and apply the tropical cyclone tracks that are provided by WindRiskTech (2019) is provided below.

Seven CMIP6 GCMs (Cesm2, EC-Earth6, Miroc6, Mpi6, Noresm6, and Ukmo6)are used to model future projections of tropical cyclone activity. WindRiskTech selects the model set and specifications (Table 4). WindRiskTech possesses downscaled GCM simulations from models, which it has determined to have a suitable representation of climatic conditions required to study tropical cyclone hazards. These models carry equal weights in our full tropical cyclone hazard ensemble.

WindRiskTech uses a dynamical downscaling technique to incorporate the large-scale conditions which drive tropical cyclone behavior and intensity from climate models (both reanalysis models and GCMs). Using these large-scale conditions, they simulate many events. The tropical cyclone simulation model is calibrated for each climate model so that the average frequency of total tropical cyclone generation over 2000-2020 matches that of the observed historical record for each basin. In the projection periods, changes in the large-scale climate conditions in the GCMs drive changes in tropical cyclone activity. Figure 2 shows the maximum 1-minute sustained wind speeds for historical global tropical cyclone tracks from the International Best Track Archive for Climate Stewardship (IBTrACS) (Knapp et al., 2018), against which the GCMs are calibrated.

Table 4. Specifications of models for tropical cyclone activity

Model element	Model specification
Vintage of WindRiskTech tropical cyclone track model	January 2022
Reanalysis models used to characterize historical storm activity	NCEP Reanalysis 2 (NCAR) ERA5 (ECMWF)
General circulation models (GCMs) used to characterize future storm activity	EC-Earth 3; EC-EARTH (2019) MIROC6; Shiogama et al. (2019) MPI-ESM1-2-HR; von Storch et al. (2019) MRI-ESM2-0; Yukimoto et al. (2019) NORESM2-LM; Seland, Ø. et al. (2019). UKESM1-0-LL; Tang, Y. et al. (2019) CESM2; Danabasoglu, G. (2019)
Modeled tropical cyclone tracks	53,025 tracks, originating in any global tropical cyclone basin, which pass within a US-specific filter, created by buffering the US coastline 50km. Approximately 65% and 35% of the tracks are for low and high intensity storms, respectively (see stratification information below). The significant majority of these tracks originate in the North Atlantic basin, though we also model storms originating in both the eastern and western Pacific.
Intensity stratification	In addition to our usual set of storms with intensities reaching tropical storm designation or above, we worked with WindRiskTech to develop a set of high intensity storms which help us characterize the extreme end of the distribution with a greater number of individual events. The relatively lower frequency of these storms compared with the

	all-intensity set was accounted for when computing summary statistics such as annual maximum observed water level.
Historical period track sources[1]	1979-1999; 3,150 tracks[2]
Current period/calibration track sources	2000-2020; 3,150 tracks
Projection period and bias correction track sources	2000-2030,[3] 2079-2099; 46,725 tracks[4]
Time series simulations	1,000 independent simulated time series per scenario

In the historical period track source, climatological data availability is limited to post-1979 due to lack of satellite data to drive reanalysis pre-1979. Note this is labeled as “1980” elsewhere in the documentation. Historical and current period storms prior to 2005 are run with 2005 sea levels. Fifty tracks/model/year for all tropical cyclones, plus an additional 25 tracks/model/year for high-intensity tracks, for each of the two reanalysis models and 21 years are used.

In the projection period and bias correction track sources, the 2000-2030 range includes two periods used in our methodology: the 2000-2019 “current” period and the 2010-2030 “2020” period. Note that these two periods share some years. Fifty tracks/model/year/emissions scenario for all tropical cyclones, plus an additional 25 tracks/model/year/emissions scenario for high-intensity tracks, for each of the 7 GCMs and 89 scenario-years (15 years [2000-2014] with 1 emissions scenario [GCM historical], and 37 years [2015-2030 and 2079-2099] with 1 emissions scenarios, RCP2-4.5) are used.

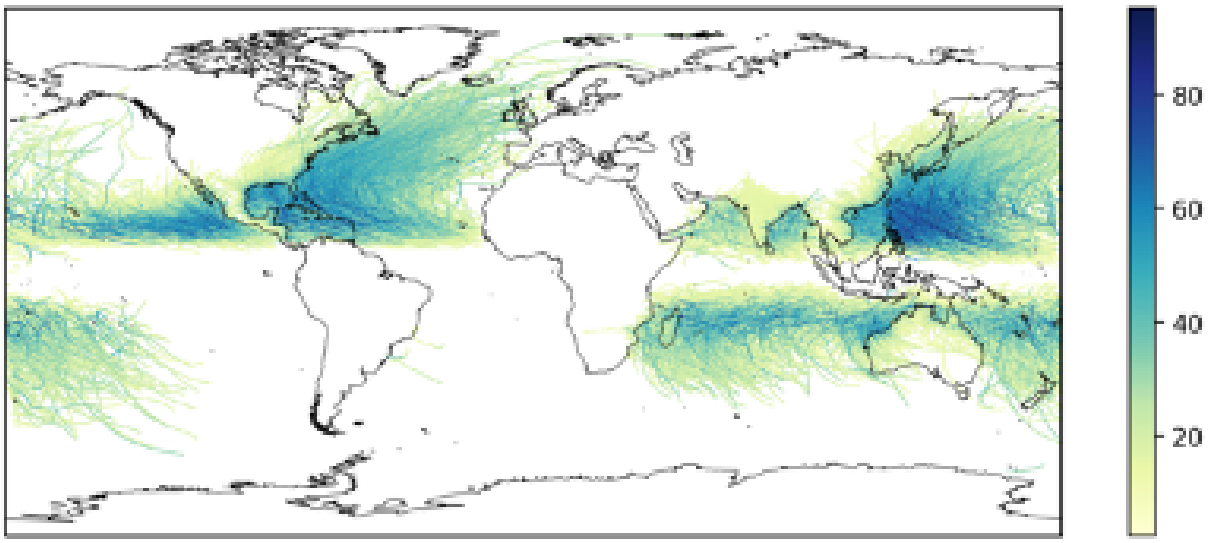

Figure 2. Maximum 1-minute sustained wind speeds (Meters per second) for historical global tropical cyclone tracks

To ensure complete coverage of extreme events in each location, we supplement each track delivered by WindRiskTech by generating two additional synthetic tracks. In each time step of each event, we apply a random deviation, with the magnitude and direction of the deviation statistically calibrated (a directed random walk algorithm). Additionally, we sample from a distribution of storm characteristics, including radius and central pressure, where the distribution shape is defined by parameters in the WindRiskTech data.

We use the GeoCLAW model (Clawpack v5.6.1 (ClawPack development team; Mandi et al., 2016), GeoClaw v4.5 (Berger et al., 2011), AMR-Claw v5.6.1 (Berger and LeVeque, 1998), PyClaw v5.8.0 (Ketcheson et al., 2012)) to simulate storm surges for each simulated track. The GeoCLAW model is calibrated by training it on NOAA tide gauge observations during historical storms, and additional wave run-up is modeled using a statistical model relating storm surge and windspeeds to observed max water levels from USGS. All storms from 1950 to 2018 with valid tide gauge data—121 total—were used to calibrate the surge model. Tide runup was calibrated with the seven storms with a significant surge which have high water mark survey data available from USGS (i.e., Florence, Harvey, Ike, Irma, Katrina, Matthew, and Sandy).

When modeling storms associated with GCM simulations of projection periods, storms are sampled such that a Poisson distribution characterizes the distribution of storms per period. We pair each simulated set of storms with a time series of sea level projections randomly sampled. Sea level change is linearly combined with storm tide and runup. Water levels during storms are tracked at each 0.1 x 0.1 degree cell within the storm's domain. The final tropical cyclone hazard model has a spatial resolution of 0.1 x 0.1 degrees.

For generating tropical cyclone-deriven rainfall intensities, we employed the rainfall generation algorithm built upon a physics-based model (Lu et al., 2018). The algorithm and its performance is validated by a comprehensive evaluation scheme against radar and gauge data (Feldmann et al., 2019). For more technical information, please refer to the aforementioned literatures.

2.3 Hydraulic and Hydrology Models

2.3.1 Hydrodynamic Model

Overview

LISFLOOD-FP, the hydraulic model, is a grid-based two-dimensional shallow water model capable of simulating water flow over a high-precision digital elevation model (DEM). A novel simplified implementation of the shallow water equations (Bates et al., 2010) yielded an algorithm for which the minimum stable time step scales linearly with decreasing grid size, rather than quadratically as had been the case with previous diffusion wave formulations (Hunter et al., 2005). Furthermore, improvements to the software implementations of shallow water algorithms through vectorization and OpenMP parallelization on central processing units (Neal et al., 2009, 2010, 2018) have yielded dramatic reductions in model runtimes totaling several orders of magnitude relative to original serial variants. The model represents channels using a 1D "subgrid" formulation (Neal et al., 2012) that enables river width to be decoupled from the model grid scale and therefore allows any river size to be represented within the model. An extended slope-dependent form of the constant-velocity routing method (Sampson et al., 2013) in conjunction with a Froude- limiter ensures that the model solution remains stable in areas where the shallow-water equation

assumptions of gradually varying flow are violated (e.g. steep or discontinuous terrain). All hydraulic simulations within this project have been undertaken on a 1 arc-second (~30m) grid.

NHDPlus Hydrography

The hydrography for the contiguous U.S. was generated by means of the National Elevation Dataset (NED) (Gesch et al., 2009), which is a high precision ground surface elevation data, and the National Hydrography Dataset (NHDPlus) (Simley et al., 2009), a feature-based database that interconnects and uniquely identifies the stream segments or reaches that make up the U.S.'s surface water drainage system. The new hydrography (UShydro) captures main channels and river streams at ~90 m (at the equator) resolution and extends the current coverage of the NHDPlus data set beyond its coverage. The new data set was created using a framework that automatically conditions the DEM and calculates flow direction and flow accumulation maps, taking into account existing inland basins in the U.S. The automatic computational framework allows replication of this methodology with different sources of terrain and river vector data sets. It's anticipated that the UShydro will expand the current research carried out on river hydrology in the contiguous U.S. The methodology used in the incorporation of UShydro relied on the National Elevation Dataset (NED) (Gesch et al., 2009) at ~30 m (at the equator) as the terrain source. The NED dataset was subsequently upscaled to ~90 m (at the equator) using bilinear interpolation. Additionally, UShydro used the NHDPlus (Simley et al., 2009) to geolocate main rivers and channels. In particular, the entire NHDPlus database was downloaded from the USGS servers in a stand-alone file in Geodatabase format. In order to facilitate the data processing, the Geodatabase was filtered and only the "NHDFlowline_Network" features were extracted in a stand-alone file in GeoPackage format. From the resulting GeoPackage file, the attribute "DivDASqKm" or Divergence-routed drainage area was extracted as a raster file using the "gdal_rasterize" program from the GDAL geospatial library (www.gdal.org).

Both the upscaled NED terrain data and the rasterized divergence-routed drainage area were re-projected from NAD83 projection to WGS 84. Also, in order to facilitate the data processing, the raster files were tiled into 5 x 5 degree tiles in both datasets, resulting in a 72-tile mosaic for the entire U.S. It is important to mention that it was decided to process the data in this form in lieu of processing the entire datasets at once due to computational expense considerations. The tiling of

the data simply allows for more efficient management and processing of the raster files, but the native resolution of the data is preserved in the tiling process.

The flow direction map was created using an algorithm that indicates the direction of the lowest elevation within a 3 x 3 cell kernel (O'Callaghan and Mark, 1984). Even though the resolution and accuracy of the NED dataset were enough to let the algorithm identify where the main rivers and channels are, in some cases, a second source of data was used (such as in the case of the divergence-routed drainage area). The divergence-routed drainage area corresponds to the drainage area of a particular cell. Thus, the headwaters cells in a basin have a value of 0 km^2 while the outlet has a value corresponding to its drainage area (e.g., Colorado River 618,000 km^2). The divergence-routed drainage area was directly burned into the NED tiles to create a new synthetic elevation following the equation here:

$$E = \frac{10}{\frac{log\,(N)}{log\,(1.5e^{-2})} - 99}$$

Where, E is the new value to be burned in the NED dataset and N is the drainage value obtained from NHDPlus. This procedure of burning main rivers and channels in a DEM is referred to as DEM Conditioning and it has been widely used to produce flow direction and flow accumulations maps (Yamazaki et al., 2019).

The equation provides new values for terrain elevation (in meters) along the channels based on the drainage area as input (km^2). The divergence-routed drainage area in NHDPlus provides, indeed, upslope areas. However, they cannot be used directly to produce a hydrography as it presents channel connectivity issues. To solve the connectivity issues in NHDPlus, the solution is to "burn" NHDPlus into NED to obtain new hydrography. The process of burning channels into a DEM has been very well studied. Basically, it assigns "new" elevation values in the DEM. Our methodology used the equation mentioned before to obtain sensible elevation values. For example, in a cell with a divergence-routed drainage area (from NHDPlus) with 700,000 km^2, the equation will produce an elevation of -95.28 m. As the drainage area increases in the downstream direction, the new elevation value will change accordingly. The equation was needed as it helps to handle very high drainage area values. Our methodology used the D8 flow method instead of D_trig as most continental-scale hydrographic datasets (HydroSHEDS, MERIT Hydro) use the D8 scheme. More

complex flow direction methods (D16, D-infinity, and D-trig) can be considered perhaps in a post-processing stage.

The previous procedure successfully captures the main rivers and channels from the NHDPlus database in addition to channels not depicted by the NHD in most of the rivers flowing within the U.S. However, the NHDPlus database does not contain complete information beyond the U.S. in trans-national rivers such as the Columbia, Rio Grande, and Colorado Rivers, which share territory with Canada and Mexico. To tackle this issue, the main channels and rivers from NHDPlus were fused with MERIT Hydro (Yamazaki et al., 2019) to complete the missing information for trans-national rivers. Additionally, the same fused vector lines were also used to identify center lines in the Great Lakes area. Endorheic or inland basins are rivers that normally retain water and do not allow outflow to other external bodies of water. It is essential to identify those correctly, or the hydrography could result in an improper drainage area for a nearby river. This problem arises as the inland basin could be seen by the flow direction algorithm as a new channel of a main river, which is not the case. To address this problem, the inland basins with the aforementioned hydrographic characteristics were detected from the NHDplus and corrected through a feature called “Sinks,” and assigned as NODATA value in the conditioned NED.

With the NED dataset conditioned using NHDPlus and MERIT Hydro data, a flow direction map for every tile using the D8 method (O’Callaghan and Mark, 1984) was used. To complete this task the RichDEM library (richdem.readthedocs.io) was incorporated into the methodology. Unlike flow directions that can be easily calculated due to the use of 3x3 cell kernels, flow accumulations cannot be calculated so easily. Resulting flow direction tiles require an efficient algorithm that efficiently connects flow direction tiles when calculating the draining area as rivers are mostly contained in different tiles. To tackle this issue, a parallel flow accumulation algorithm with efficient memory management was used (Barnes, 2017).

The hydrography for the contiguous U.S. was generated by means of the NED and the NHDPlus. The new data set extends the current coverage of the NHDPlus for trans-national rivers, has a resolution of ~90m (at the equator), and is distributed in GeoTIFF format using 72 tiles of 5x5 degrees which mosaic the entire contiguous U.S. with flow direction and flow accumulation. This standard framework allows for a replicable approach that can be easily used with other data

sources of terrain elevation and vector data, and the framework is computationally efficient as the entire computational chain took ~6 hours to obtain a flow accumulation map.

Hydraulic Channel Solver

A critical control on how water moves through a landscape for any riverine model is the definition of the river channel network. In the case of fluvial flooding, the river channel is usually the main conveyor of discharge and will interact with the floodplain in a complex manner as water moves both from and to the channel in a manner dependent on local variability in topography and friction. Even in the case of other types of flooding, such as pluvial and fluvial, the role of channel conveyance can be significant. How channels are represented in a regional scale flood model will therefore influence inundation simulations, particularly at low return periods where small changes in river conveyance can have a disproportionately large impact on the simulated flooding. For traditional hydrodynamic modeling, the quality of river bathymetry data is key to accurate simulation of the relationship between discharge and water level. However, since high-quality versions of such data are not available for national scale modeling contexts, an approximation must be used that best represents the water surface elevation and discharge relationship given the available data. The framework used in approximating this relationship is a 1D gradually varied flow assumption to estimate depth along the channel network.

This is governed by the equations:

$$\frac{\partial h}{\partial x} = \frac{\left(S_0 - S_f\right)}{1 - Fr^2}$$

where, h is depth, x is distance downstream, Fr is the Froude number, S_0 is the bed slope, and S_f is the friction slope. We assume that the river channel is rectangular and that friction is represented by Manning's equation such that friction slope is found via:

$$S_f = n^2 \left(\frac{Q}{wh}\right)^b \left(\frac{wh}{2h + w}\right)^{-\frac{4}{3}}$$

where, n is manning's roughness coefficient w is the channel width and Q is discharge. The Froude number of the channel Fr is then

$$Fr = \frac{Q}{w\sqrt{gh}}$$

where, g is acceleration due to gravity. For any set of bed elevations (z), the gradually varied flow profile is found by solving these equations using the Runge-Kutta method. A first-order approximation of bed elevations is made by subtracting depth from the bank height profile, where pixel-wise river depths are estimated by using Manning's equation rearranged for depth.

$$h_{bf} = \left(\frac{nQ_{bf}}{S^{0.5}w}\right)^{\frac{3}{5}}$$

where, S is water surface slope approximated by the DEM slope and Q_{bf} is calculated using the RFFA for an assumed bankfull discharge return period (typically, 1-in-2-year).

Due to backwatering effects, these initial bed elevations result in an overprediction of the water surface elevation at bank full discharge for all river reaches where diffusion of shallow water wave properties are important (most lowland rivers and deltas). Thus, we seek bed elevations that minimize the least squares difference between the desired water surface profile at bank full discharge and the simulated profile by solving the gradually varied flow. This can be done via least squares nonlinear estimation; however, the computational cost of optimizing all bed elevations is too high for a continental-scale application meaning a simpler bed nudging approach is used in practice. The nudging result is channel bed and bank estimates that are consistent with both the DEM and the return period discharges at which overbank flow is to commence. Thus, this method creates a set of channel network geometries that behave according to the assumptions of bankfull return period imposed by the model user.

2.3.2 Hydrologic Models

Two hydrologic models are employed for different purposes, the Hydrologiska Byråns Vattenbalansavdelning (HBV) for modeling watershed streamflow in fluvial flood modeling and the

Horton Infiltration Model for simulating direct runoffs (i.e., effective rainfall) in pluvial flood modeling.

HBV model: Lumped watershed streamflow simulation model

HBV is a simple conceptual hydrologic model able to simulate a change in streamflow by time for a given watershed with a specified outlet (Bergstroem, 1992; Seibert and Vis, 2012). HBV was chosen because of its flexibility, computational efficiency, and proven effectiveness under various climatic and physiographic conditions. Also, it has been extensively used in climate impact studies across a wide variety of catchments and scales (Akhtar et al., 2008; Bergström et al., 2001; Cloke et al., 2013; Hinzman and Kane, 1991; Seibert, 1997; Smith et al., 2014; Teutschbein et al., 2011). It is also computationally efficient, which is vital when carrying simulations at these scales with multiple scenarios and models.

HBV was set up and parameterized for each selected basin using the global regionalized parameterization provided in Beck et al. (2016). The model uses a total of 14 parameters and requires only daily precipitation and daily minimum and maximum temperature as forcing data to simulate most components of the hydrological cycle (e.g. evaporation, groundwater, soil moisture, snow water equivalent, etc.) needed to obtain output discharge. HBV was set up to simulate historical discharge time series at river locations of outlet points of all selected basins. HBV forcing data for each basin were taken from the Daymet data product (https://daymet.ornl.gov/), which is derived from a collection of algorithms designed to interpolate and extrapolate from daily meteorological observations to produce gridded estimates of daily weather parameters, including minimum and maximum temperature and precipitation, produced on a 1 km^2 gridded surface.

HBV has previously been tested for its performance in Arctic basins and basins affected by significant snowmelt processes. The routine which calculates snowmelt and refreezing is based upon a simple degree day method. A threshold temperature defines the temperature for snowmelt. This threshold temperature also determines if the precipitation will be treated as rain or snow, and thus snow accumulation can be simulated. During the spring melt, the threshold temperature functioned to control the initiation of the simulated snowmelt. Hinzman and Kane (1991) found that the model functioned well but is sensitive to the threshold temperature, TT, and a parameter in the transformation function, MAXBAS. These parameters need to be adjusted to reflect snowpack properties which vary from year to year. The initiation of melt could be controlled by TT, and the

amount of snow damming is affected by MAXBAS. To account for these parameter sensitivities and sensitivities of other parameters, we opted to run HBV in an uncertainty framework by computing thousands of simulations for each basin selected, with each simulation using different parameter set values.

Horton infiltration model

Horton defined infiltration capacity as the maximum rate at which a given soil can absorb rainfall when the soil is in a specified condition. Based on observations of infiltration in the field, Horton developed an infiltration model accounting for the decrease in infiltration capacity over time due to flow-restricting changes occurring in a thin layer at the soil surface. Building on this conceptual framework, Horton developed what came to be known as the Horton infiltration equation:

$$f_p = f_C + \left(f_O - f_C\right) e^{-kt}$$

where f_p is the infiltration capacity (depth/time) at some time t, f_c is a constant minimum value of infiltration capacity which f_p approaches asymptotically, f_O is the initial infiltration capacity at the start of the infiltration event, and k is a constant which controls the rate at which the infiltration capacity decreases as a function of time, t.

The model has been widely used in hydrology and related disciplines, and its success may be due to the correctness of its underlying conceptual framework or the flexibility of its mathematical form, or some combination of the two. The main deficiencies of this infiltration model are that the parameters are not certainly related to measurable physical properties of the soil, and more importantly, the model's conceptual framework fails to include the most fundamental reason that infiltration rates decrease over time. That fundamental discovery had, in fact, been made decades before but apparently was not widely accepted in Horton's time.

2.4 Hazard Layer Creation

2.4.1 FSF-FM Execution

Once all inland and coastal metadata has been updated and climate adjusted, inputs can be created to run every desired scenario in the FSF-FM. Fig. 3 depicts the chosen scenarios for the new version. The pluvial, fluvial, and coastal components contain low, median, and high currents. The continental United States is composed of 933 inland tiles (see Fig. 4), 34 East Coast tiles, and 9 West Coast tiles based on their latitude and longitude. These tiles and their simulations can be run in any order or combination. Inland tiles measure 1.25° by 1.25°. Coastal tiles are much larger and irregularly in size until after post-processing.

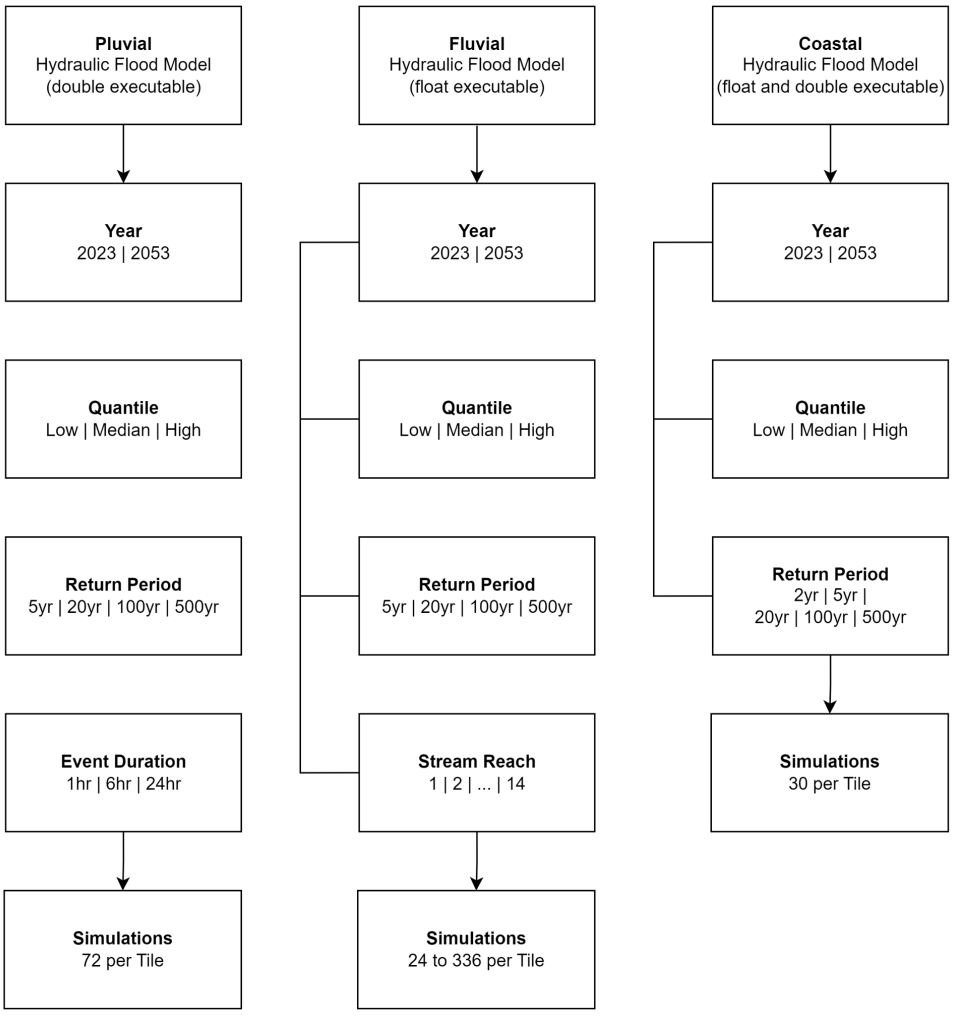

Figure 3. Scenarios for each maximum water surface elevation output for current (2023) and future (2053) scenarios

The 5, 20, 100, and 500-year return periods are modeled, and coastal also includes the 2-year return period. Pluvial simulations contain 1, 6, and 24-hour durations, resulting in 72 simulations for each tile. Fluvial simulations consist of stream reaches, which can vary from 1 to 14. Therefore fluvial simulations can range anywhere from 24 to as many as 336 simulations for each tile. There are simply 30 simulations for each coastal tile since there are 30 different scenario combinations and no durations or reaches.

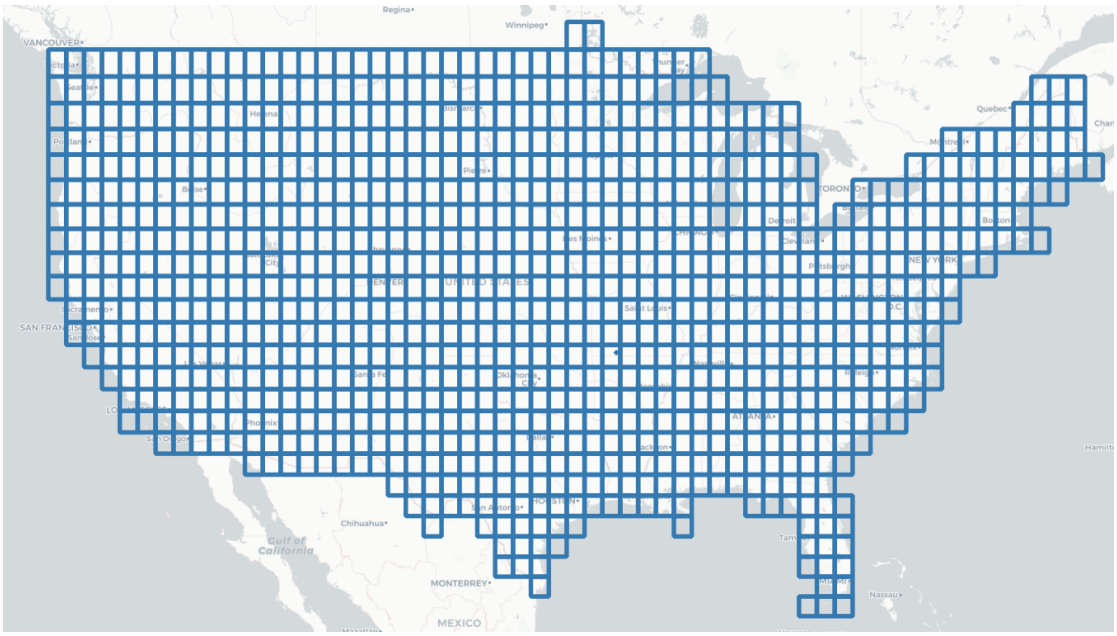

Figure 4. A map of 1° x 1° inland tiles

2.4.2 Post-processing

Framework

The FSF-FM produces a multitude of maximum water surface elevation outputs in the form of raster files. These grids include the maximum water depths in each pixel over an entire simulation of time steps. The outputs represent specific scenarios separated by durations (pluvial), which must be combined, and stream reaches (fluvial), also to be combined. These outputs are created as overlapping tiles that will be blended and cropped. Adaptations were incorporated into the inland portion before running the model, but coastal adaptations are added before they are cropped. Fig.

5 displays this workflow.

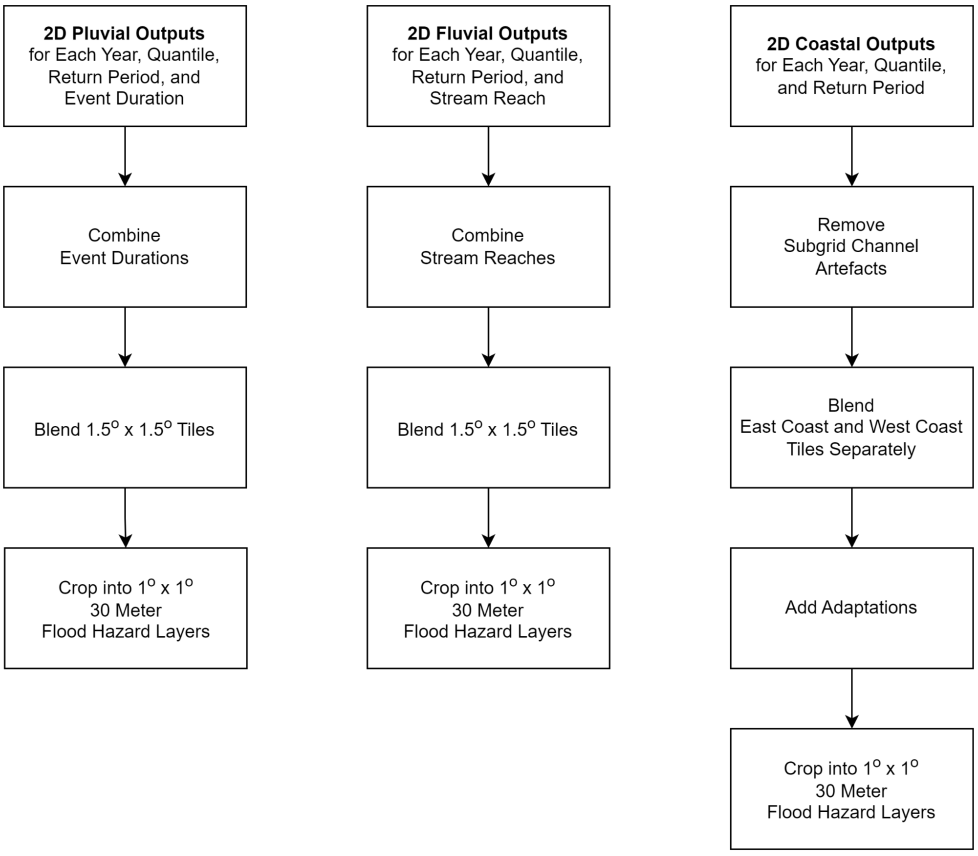

Figure 5. A workflow of the inland and coastal post-processes

Combining, Blending, and Cropping

Inland post-processing consists of processing 2D pluvial and fluvial outputs into flood hazard layers. Pluvial scenarios contain 1-hour, 6-hour, and 24-hour event durations. All pluvial durations for a single scenario and return period are combined to create a single pluvial hazard layer. Fluvial scenarios contain stream reaches. Similarly, all reach for a single scenario and return period are combined to create a single fluvial hazard layer. Once all simulations of a scenario are combined, the water depths are converted to water surface elevation and recalculated over the DEM without the Sub-grid channel cells. The result is one hazard layer for every year, quantile, and return period scenario.

The initial output layers are 1.5° by 1.5° tiles. The 0.25° edge of each tile must be blended to create a seamless hazard layer with minimal boundary artifacts. After blending, the tiles are cropped into 1° by 1° tiles. The final inland product is made up of 933 post-processed tiles with 30-meter resolution for each year, quantile, and return period combination.

Coastal post-processing

Coastal tiles require a post-processing that involves processing 2D outputs into blended flood hazard layers, but each tile varies in size due to irregular coastlines. The East Coast and West Coast are processed separately. Sub-grid channel artifacts are removed before overlapping tiles are blended. Adaptations, such as levees, are overlaid on the flood hazard layer. Finally, the layers are cropped into 1° x 1° tiles for data analysis.

Downscaling and Monotonicity

All fluvial, pluvial, and coastal hazard layers undergo two final processes before handing them over to the data team for analysis (see Fig. 6). Using the highest resolution available, the 1/9 arc-second (3-meter) National Elevation Dataset (NED-3) from USGS, along with 3-meter water surface mask data, the layers are downscaled from 30-meter output to this fine resolution for developing property-level flood hazard layers. Second, these high-resolution flood hazard layers are passed through a monotonic function to ensure the water surface decreases downstream across each scenario and return period.

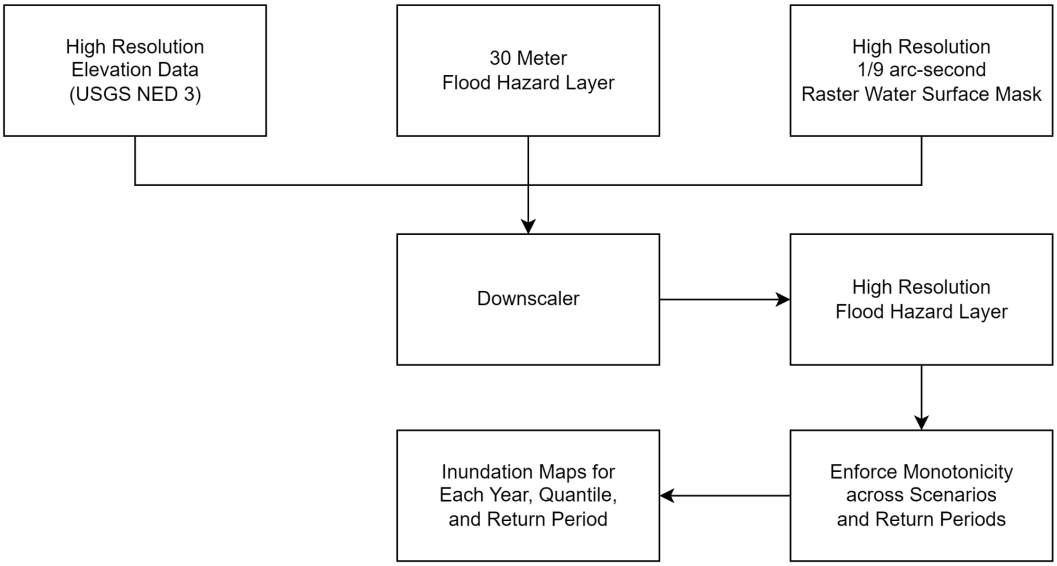

Figure 6. A workflow of the downscaling and monotonicity processes

Before downscaling, a fluvial depth threshold of 5 cm and a pluvial depth threshold of 20 cm are enforced. This inhibits fluvial flooding below 5 cm and pluvial flooding below 20cm to appear on the final hazard layers. Future versions will most likely adjust the pluvial threshold to 5 cm as well. These thresholds were implemented as the FSF-FM cannot accurately model flooding at this level of precision.

The downscaling process begins by creating buffers around the water surface elevations using dilation. This process subtracts the high-resolution elevation from the water surface elevation to obtain depth. The extended water surface elevation mask is resampled to produce a new high-resolution depth layer.

Monotonicity is the final process of the FSF-FM. In some rare instances, the model produces flooding in lower return periods unseen in higher return periods. For example, consider Fig. 7. This particular area contains flooding in the 5-year return period (left) but not in the 20-year return period (right). Since flooding is nonexistent in the higher return period, it must be removed from the lower return period. Fig. 8 shows this removal from the 5-year return period. The monotonic function preserves this order first by comparing the 75th quantile across 25, 50, and 75 quantiles, and then in the return periods, but the 2023 and 2053 outputs are processed separately.

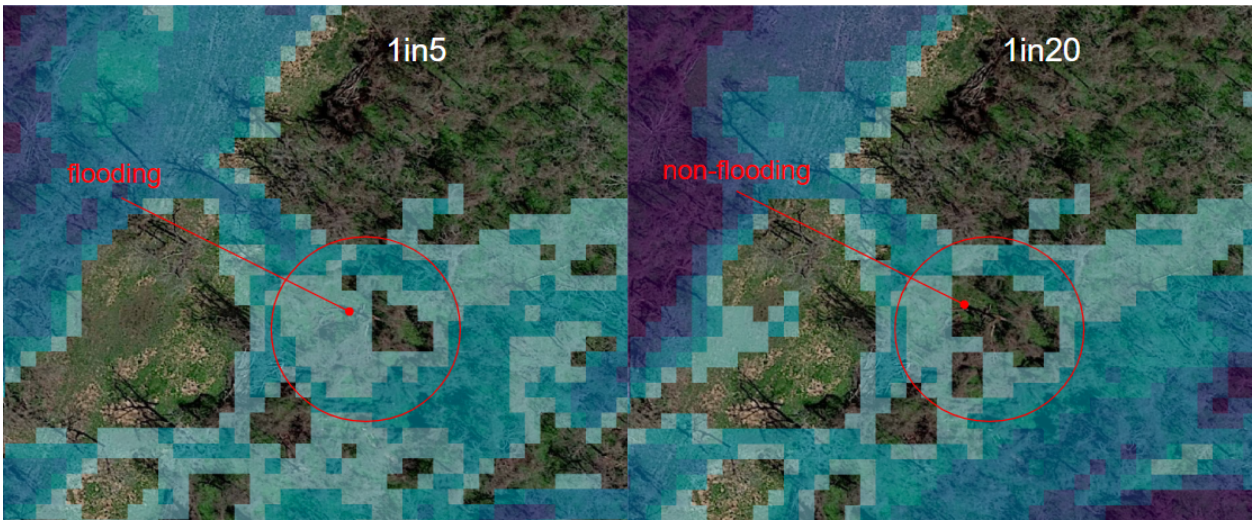

Figure 7. Before monotonicity: flooding appears in a 5-year return period but not a 20-year

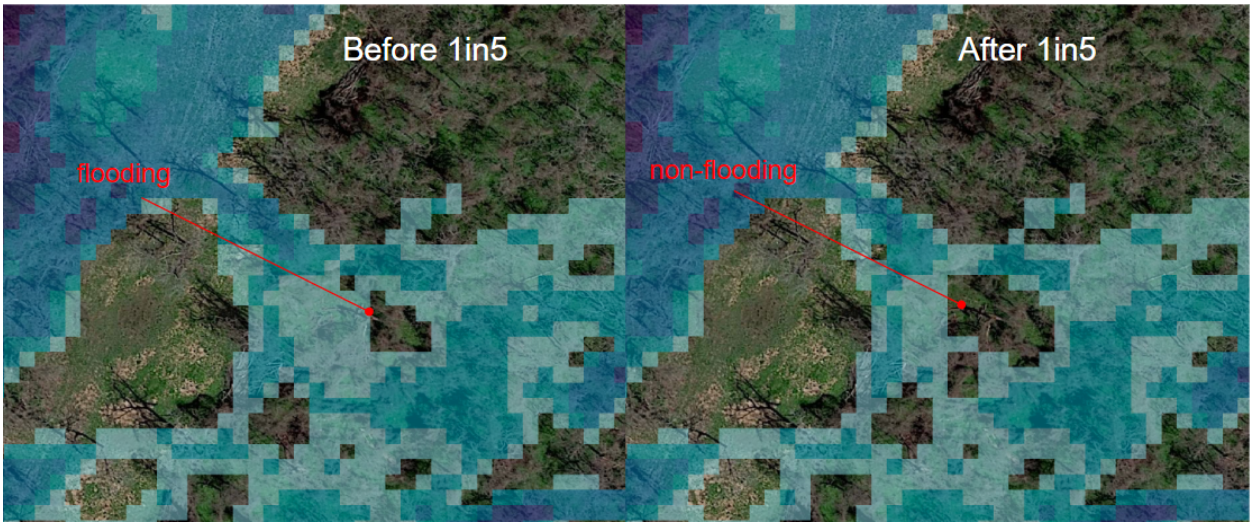

Figure 8. After monotonicity: flooding removed from a 5-year return period

The FSF-FM produces monotonic pluvial, fluvial, and coastal flood hazard layers to pass forward to FSF's Data Team for analysis, quality assurance, and further processing. There are 24 pluvial and fluvial scenarios, with almost all containing 933 tiles. There are 30 coastal scenarios, with almost all containing 131 tiles.

3. Pluvial Flood Risk Modeling

3.1 First Street Foundation Precipitation Model (FSF-PM)

3.1.1 Methodology

Data

The Automated Surface Observing System (ASOS) is used in the development of the FSF-PM as the primary precipitation record source for implementing Regional Frequency Analysis at station-level. ASOS is a well-known weather observation system with more than 913 operational observation stations in the U.S. that provide high temporal resolution data. A 60-minute precipitation measurement of ASOS is used as the primary data to develop the FSF-PM for 1, 6, and 24-hour durations. ASOS data from 2002 to 2021 are used; we believe the period represents the current climate circumstances (Kim et al., 2022). ASOS data is available from the online site (https://mesonet.agron.iastate.edu/request/asos/1min.phtml).

The gridded daily precipitation products from the Parameter-elevation Regressions on Independent Slopes Model (PRISM) group are used for developing a new atlas of precipitation frequency estimates (PFEs). The PRISM Climate Group provides a variety of spatially distributed climate variables in the United States based on a long-term period of ground-based and remote-sensed (e.g., weather radar) observation data. Since 1 January 2002, weather radar measurements have been used for daily modeling.

To generate a climate variable map, they employ the interpolation method called PRISM, which uses the observation data, a digital elevation model, and other geographic data resources to generate gridded estimates (a horizontal resolution of 0.00833 degrees) of climatic parameters at various time scales (Daly et al., 1994; 2017). PRISM should be considered "stable" (unlikely to change until a significant version changes). As comparable mapping approaches, the spline techniques are recommended as good options, developed primarily by Wahba (1980). The method allows for spatially variable dependence on elevation, suitable for applications across large heterogeneous areas. The ANUSPLIN package, a program employing a multi-dimensional Laplacian partial thin plate smoothing spline technique, is a good framework for developing a

precipitation estimate map (Hutchinson and Bischof 1983). The MT-CLIM model (Running et al., 1987) is another option, applying an inverse distance weighting technique to extrapolate meteorological variables from the point to the grid of interest, making corrections for differences in elevation, slope, and aspect based on a user-specified domain-wide lapse rate for the precipitation-elevation relationship (Stillman, 1996).

The PRISM daily precipitation data is used as a predictor in mapping the gridded PFEs. It is because their daily precipitation well represents its spatial and temporal variabilities by geomorphological and climate features, and directly employing the data is more straightforward. The same period of the PRISM data with the ASOS data is used to consider a consistent period of precipitation record.

Framework

Before the primary analyses, the pre-processing to fill missing data and detect/remove outliers was implemented for the ASOS data. A simple interpolation method using a time window as a parameter was employed to fill missing data. Outliers were detected using the interquartile range (IQR) method to define outliers' upper and lower bounds. The IQR method has a scale factor to adjust the bounds and is 1.5 in general. This study considered the scale factor for only the upper bound and determined it based on a sensitivity analysis (scale factor = 5.0). Detected outliers were removed and replaced with the interpolated value. One-minute precipitation of ASOS was accumulated and converted to 60-min duration precipitation.

In the validation of the Atlases, the annual maximum series (AMS) used in the development of the Atlas 14 in Texas was employed since the latest period of AMS data is available up to 2017 (the last year of the data is 2018, but it is excluded due to the relatively few numbers of gauges). Fundamental analyses to understand a trend of the AMS, validate the selected probability distribution, and examine the effect of precipitation nonstationarity on developing IDF curves were the focus. The FSF-PM: Baseline for the historical period was developed based on the recent 20 years of ASOS data from 796 gauge locations across the contiguous United States (CONUS). ASOS was selected since the density as a single gauge observation system is comparable with the Atlas gauge network and able to provide the latest precipitation data. In the evaluation process, the difference defined as the difference percentage between PFEs from the FSF-PM:Baseline and

Atlas was used as a criterion for measuring uncertainties in the Atlas. The Atlas was paired with the FSF-PM:Baseline by sampling PFEs, collocated with the selected ASOS gauges.

Frequency analysis

Regional frequency analysis (RFA), based on the index-flood procedures, was employed to develop new PFEs from ASOS and Stage-IV precipitation data. The RFA was developed to derive more reasonable IDF curves by analyzing multi-site sampling data in a homogeneous region rather than using single-site data (Hosking and Wallis, 2002). The RFA is similar to the at-site frequency analysis, mainly consisting of the four steps: the AMS preprocessing, fitting AMS to theoretical distributions, selecting a distribution, and deriving PFEs for a specific scenario of a storm (e.g., duration and return period). However, the RFA requires a regionalization process by categorizing groups of gauges with statistical similarities. In the general RFA process, the quantile function of the frequency distribution at site is defined as follows:

$$Q_i(F) = u_i q(F), \; i = 1 \cdots N$$

where, u_i is a scaling factor defined as the index-flood, $q(F)$ is the regional growth curve as a function of ranging from 0 to 1, F is an annual exceedance probability in precipitation frequency analysis, and N is the number of gauges in a homogeneous region.

A homogeneous region, in this context, is a group of gauges with similar statistics of selected variables such as L-moments. The L-moments are an alternative system of representing the shape of distributions, and they historically arose as modifications of the conventional probability-weighted moments (Hosking and Wallis., 2002). In the index-flood procedures, a regional growth curve was derived from multiple gauge data in a homogeneous region under the assumption that the probability distributions of N-gauges are identical except for the scaling factor of each gauge. Hence, this method is beneficial for reducing uncertainties arising from a short period of record and the shortage of various extreme cases. To identify homogeneous regions, K-means was employed as a clustering method. The clustering method seeks gauges with similar characteristics and groups them as homogeneous regions. Coordinates, gauge altitude, mean annual maximum precipitation, and L-moments ratios (e.g., L-CV and L-skewness) were used as variables to cluster

groups.

A goodness-fit-test was implemented to choose the optimal probability distribution using the Akaike Information Criterion and Bayesian Information Criterion for various durations. Parameters of the selected probability distributions were estimated using the L-moment and PWM methods. For this process, the L-moments3 library in Python was used. In this study, the four 3-parameters distributions (GEV, GLO, GNO, and GPA) were considered to validate the methodology of the NOAA Atlas. For more details, readers may care to refer to Hosking and Wallis (2002), as the RFA and the associated index procedures in this study are developed based on that reference.

Mapping

A framework to develop the new First Street Foundation Precipitation Model (hereafter the FSF-PM) of PFEs based on 21st-century observations consists of four components, (a) RFA, (b) Predictor Process, (c) Mapping, and (d) Correction, as shown in Fig. 9.

The RFA is similar to the at-site frequency analysis, consisting of four steps, Annual Maximum Precipitation (AMP) preprocessing, fitting AMPs to theoretical-extreme distributions, selecting an optimal distribution, and deriving PFEs for various durations and return periods. However, it has one more step, the regionalization process. Regionalized IDF curves could be derived by considering multi-site sampling data in a regionalization process in RFA (Hosking and Wallis, 2002). The regionalization process categorizes homogeneous groups of gauges having statistical similarities. The K-means clustering method is employed to identify homogeneous groups and coordinates, gauge altitude, mean AMP, and Linear (L)-moments ratios (e.g., L-CV and L-skewness), which are used as variables to cluster groups. A goodness-of-fit test to select the best probability distribution is implemented using Akaike Information Criterion and Bayesian Information Criterion. This study follows the same regional frequency analysis as Kim et al. (2022), providing more technical details.

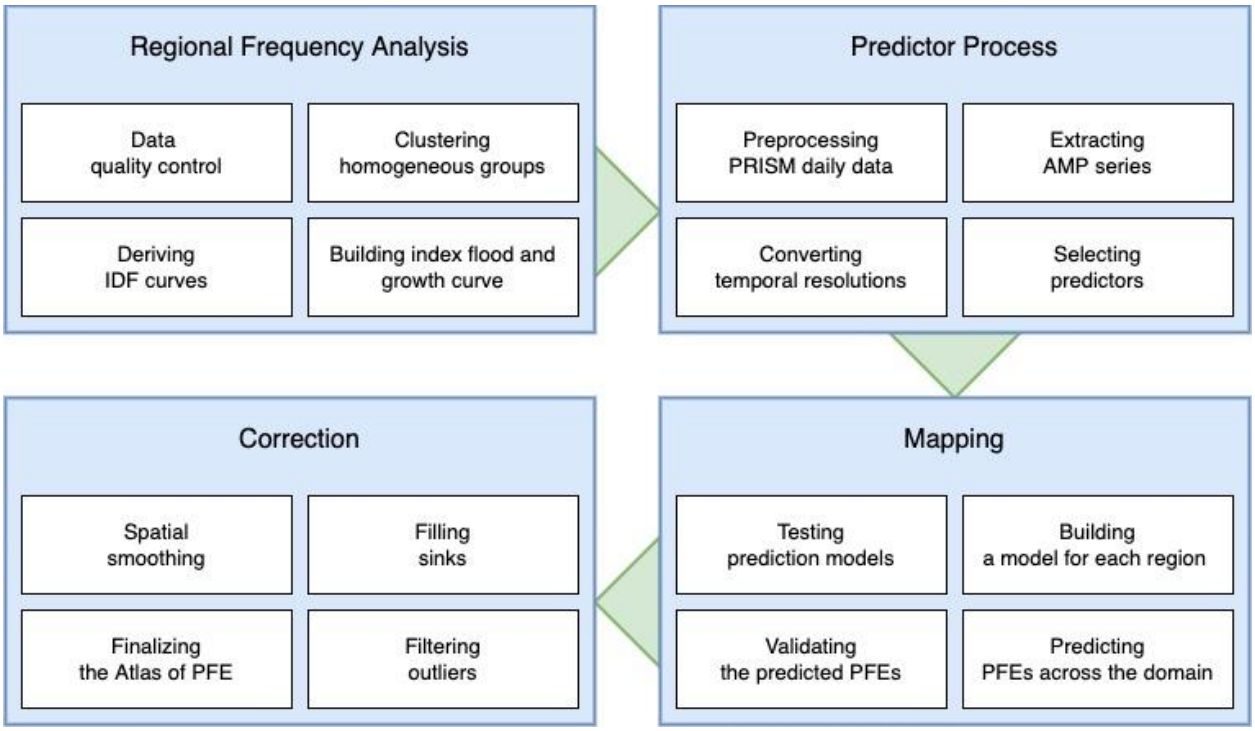

Figure 9. A framework to develop a precipitation frequency estimate map

The predictor process is to choose an optimal predictor for mapping PFEs in both gauged and ungauged areas, which is a core process of developing new gridded PFE maps in different durations and return periods. Considering the high density of the observation network and sophisticated techniques used in the development, the PRISM daily precipitation product is selected as a fundamental data source to create a predictor map.

Instead of using large-temporal-scale climatic precipitation variables such as annual precipitation as a predictor, various percentiles from the 50- to 98-th of AMPs are tested. AMPs from the recent 20-year PRISM daily precipitation data are analyzed to examine their correlation with the point-based PFEs. For sub-daily durations, 24-hr AMPs are converted to sub-daily AMPs (1-hr as the representative result) using a depth-duration curve derived from the RFA process.

In the mapping process, a linear regression model accounting for a relationship between a predictor (x) and PFE (y) is employed to predict the PFEs over CONUS. Note that we experimented with several interpolation methods, such as the inverse-distance weighted method

and ordinary Kriging. We confirmed they performed poorly in a boundary area with other countries or oceans. These methods interpolate values between the stations considering their distance (Euclidean and statistical) as weight. The performance varies with the gauge network density and could not properly predict a value in the boundary areas without stations outside the domain. Thus, this study chose a regression method employing a relationship between the point-based PFEs and PRISM's annual maximum as a predictor to predict PFEs over the domain, which is the proper approach with limited point-based PFE data and reliable gridded predictor data for mapping.

A linear regression model through the origin is built for each targeted grid using up to the nearest 30 pairs of the point-based PFEs and PRISM AMPs. Each grid cell's mapping process is implemented as a moving-window function of row and column. For example, the pointed-based PFEs are collected at a grid cell by sampling the nearest N-stations and paired with the selected AMPs. A simple sensitive analysis determines the number of stations in this study. A linear regression model is built based on the samples, and the grid PFE is predicted using the model with an AMP selected at the grid cell. This process is repeated at the following grid cell. The mapping process is implemented in the exact spatial resolution (~800 m) as the NOAA Atlas. A validation process is implemented with a control group to confirm the model performance.

Lastly, spatial filtering is implemented to remove abnormally underestimated and overestimated values compared to neighboring PFEs. A sensitivity analysis of the median filter process is implemented to choose the correct application number. A fillsink process is employed to fill null values and extrapolate inland PFEs to small island areas where the point-based PFEs and PRISM data are unavailable.

3.1.2 Comparison with the national standard

The FSF-PM is compared with the NOAA Atlas 14 in Fig. 10. From a continental scale perspective, both atlases have similar spatial patterns of PFEs, but significant differences are identified depending on regions' geographical location and topographical features, especially in the regions near oceans, the Great Lakes, and the upward slopes of mountain ranges (e.g., Coast Range, Cascade Range, Sierra Nevada, and the Rocky Mountains). Increments in magnitude and frequency of extreme precipitation were notable in those regions, mainly for 1-hr duration events. Along the West Coastline, an increase in PFE for a 1-hr duration is dominant, except for the

downward slopes of the mountain ranges where a decreasing trend is dominant. In those areas, primary sources (i.e., precipitable water vapor) driving EP events come from the North Pacific Ocean and result in heavy precipitation when they face upward hillslopes due to the orographic effect. Atmospheric Rivers are excellent examples of this event resulting in AMP (Demaria et al., 2017b; Konrad and Dettinger, 2017). Thus, the spatial distribution of the difference in the states with mountain ranges is polarized along mountain ridges.

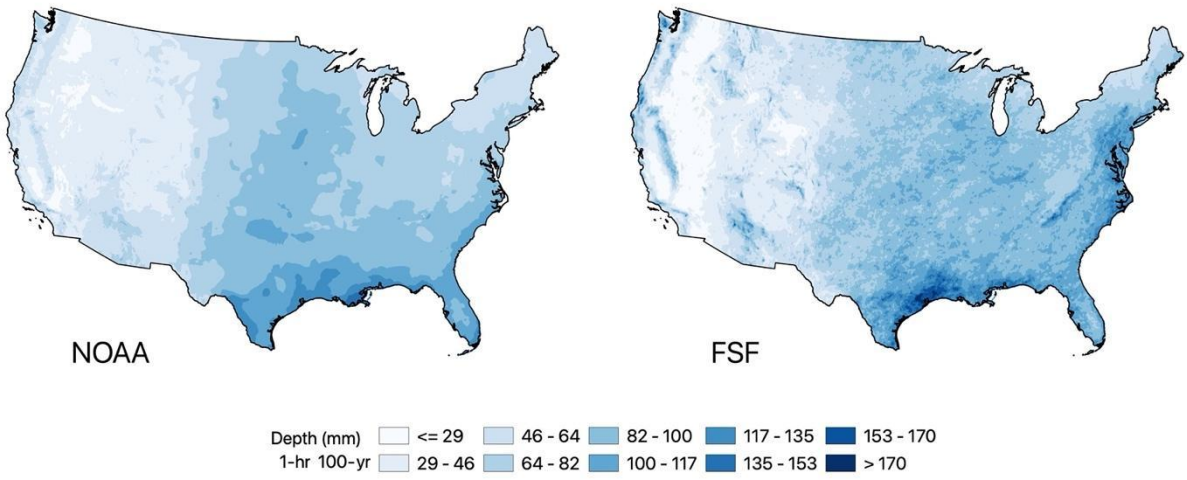

Figure 10(a): PFE maps for a 1-hr duration and 1-in-100-year return period

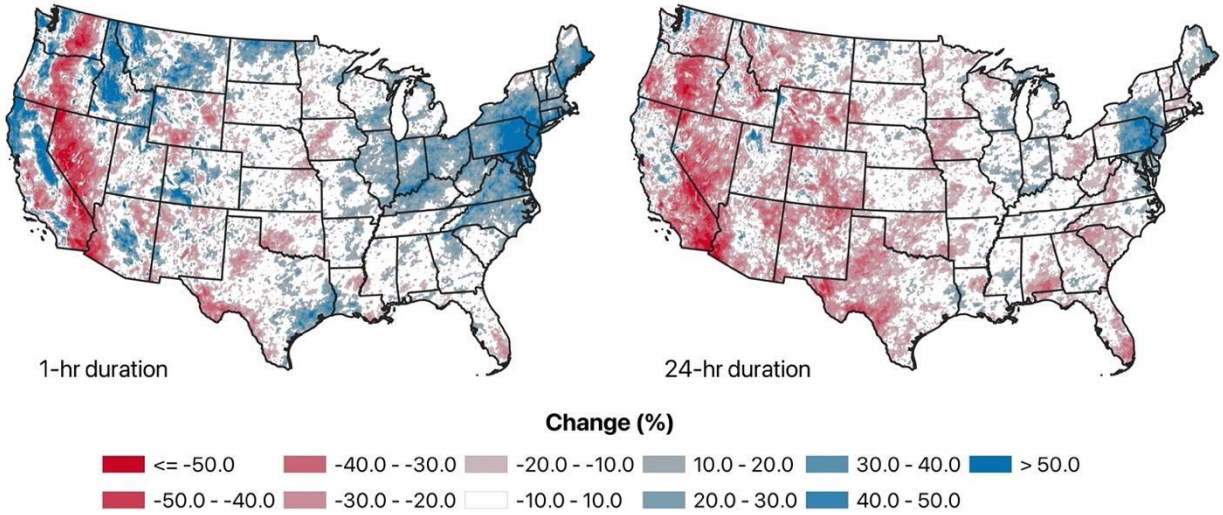

Figure 10(b): Difference maps for a 1-in-100-year return period

Figure 10. Comparison of maps of PFEs from the NOAA Atlas and FSF-PM. (a) is a comparison of two atlases for a 1-in-100-year return period and 1-hr duration. (b) shows the percent change in the

FSF-PM compared to the NOAA Atlas 14 for the same return period and 1- and 24-hr durations. The percent change is calculated from a simple equation: (FSF-NOAA)/NOAA x 100 (%).

In northwestern states like Idaho and Montana, the increment of PFEs for a 1-hr duration and 1-in-100-year return period was notable as the change was reasonably consistent statewide. Near the Gulf of Mexico, the difference in Houston, TX, and Lake Charles, LA, ranges from 20 to 40%, which is considerable—especially considering the development year (i.e., 2018) of the NOAA Atlas 14 in TX. Precipitation non-stationarity and the non-stationary method used in the FSF atlas development are the primary reasons for the difference between the two atlases in the area, even though the NOAA Atlas 14 in TX has been developed recently.

The most significant difference is in states surrounding the Northeastern and Great Lakes regions. The spatial trend of the differences is also relatively homogeneous and robust compared to the Western states. The strongest signal of the positive difference is formed around Pennsylvania, Maryland, Delaware, New Jersey, and New York, and the extent and intensity decrease further from this area. Events with tropical moisture sources and landfalling hurricanes/tropical storms were the main contributors to the increases in the frequency of these most extreme events. This is consistent with the significant increases at inland locations (Howarth et al., 2019).

The 24-hr result is slightly different from the 1-hr result regarding the spatial distribution and intensity of the difference. Except for the states surrounding the Great Lakes and the northeastern region, the 21-century extreme PFEs for a 24-hr duration tend to decrease compared to the NOAA Atlas 14. The tendency that the NOAA Atlas 14 relatively underestimates PFEs in the northwestern states is understandable since the region was developed in the 1970s with outdated records that are by now over 50 years old, meaning that the NOAA Atlas 14 of the region cannot reflect a change in EPs over the last five decades. Taken altogether, the results from 1-hr and 24-hr durations spatially signal that a change in EP features has occurred. However, a trend of heavy precipitation for a short duration (i.e., 1-hr) could be a dominant type of EP event that will lift rapid precipitation-driven threats (e.g., flash floods) in the current and future.

Fig. 11 compares the PFE profiles from the FSF-PM and NOAA Atlas along sections cut across the country, showing the elevation through the mountains. The upper panel presents PFE profiles by distance from a coastal area in Houston, TX, to Great Lakes, MI. In the coastal area in Houston,

Texas, the difference between the two PFEs (FSF and NOAA) was huge compared to other areas far from the Gulf of Mexico. The PFE profile curve from the NOAA Atlas is relatively over-smoothed, whereas the FSF-PM is relative to a change in elevation. Between Missouri and Illinois, a change in depth of the NOAA Atlas 14 was around 3% and more constant along the zonal distance, while FSF shows more significant fluctuations depending on the changes in elevation and PRISM. In addition, mountain and coastal areas and state boundaries, where two more NOAA Atlas maps (developed in different years using different periods of precipitation data) are merged, present notable differences considered as signals representing changes in EP and benefits of the FSF-PM.

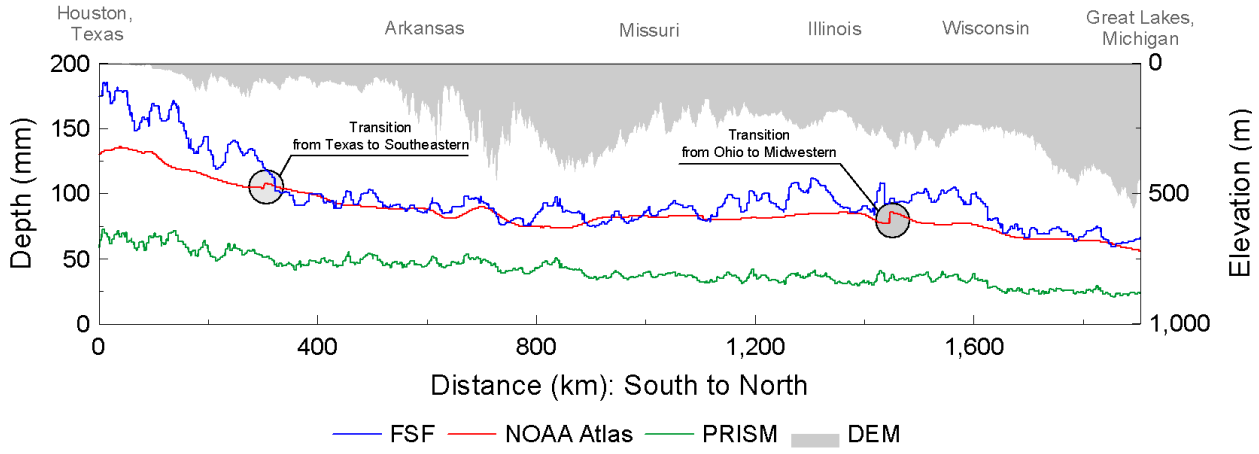

Figure 11(a): West to East

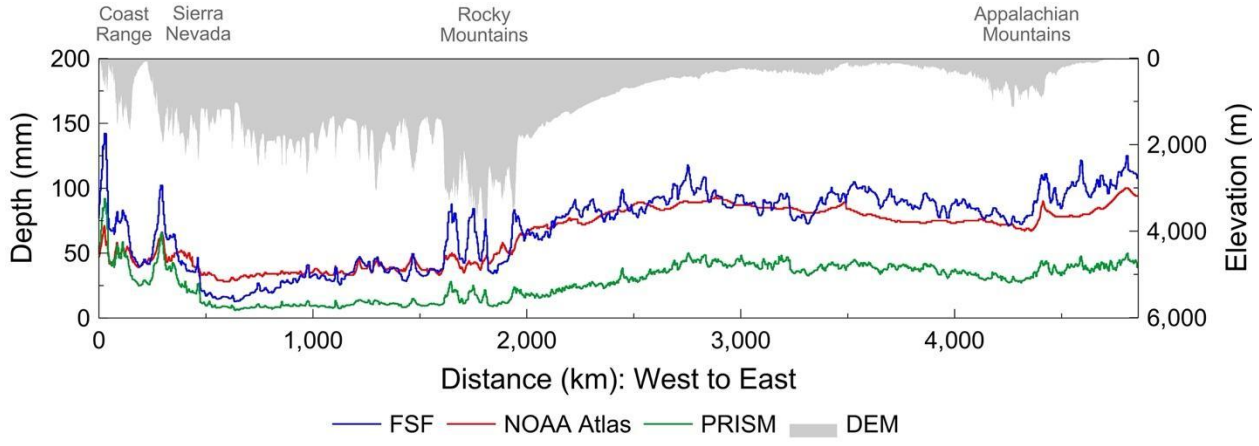

Figure 11(b): South to North

Figure 11. A profile of PFEs by distance: the upper panel is from the South to North (Lat. -95.108, Lon. 29.127: Lat. -87.931 Lon. 46.775), and the lower panel is from the West to East (Lat. 40.331,

Lon. -124.356: Lat. 36.489 Lon. -75.947). NOAA Atlas 14 (red) and FSF-PM (blue) are PFEs for 1-in-100 years for a 1-hr duration scenario. PRISM indicates the 50th percentile of a 1-hr AMP corresponding to a 2-yr return period derived from PRISM. DEM (black) indicates a profile of elevations by distance.

The lower panel (b) in Fig. 6 compares the PFE profiles along the distance from the West to the East for a particular direction that goes through the mountains. All three PFEs responding to a change in elevation were commonly observed, but the magnitudes and sensitivity to a change in elevation were different. The result near the Coast Range and Sierra Nevada is a good example of relative differences. The area is where the NOAA Atlas presents significantly lower PFEs than the others. It is comparable with the 2-yr return period PFE of PRISM instead of the 100-yr return period of the FSF Atlas. This result has been expected considering an increase in EP depth and the time windows used in the development, respectively. However, the difference between the NOAA Atlas and FSF-PM is around 50% in the front of the Coast Range and Sierra Nevada mountain areas, which is considerable.

A decrease in PFEs at the eastern aspect (or hillslope) of the Sierra Nevada range was more significant in the FSF-PM than in the NOAA Atlas. In the western U.S., direct precipitable water vapor comes from the North Pacific Ocean, and heavy precipitation storm events have been observed across the western hillslope of the mountain ranges resulting from the upslope wind and orographic effects (Salathé Jr., 2006; Adam et al., 2006; Viale and Garreaud, 2015). Also, a significant change in EP was observed in sub-daily durations but not in daily or longer durations (Kim et al., 2022).

In the region along the Appalachian Mountain range where the NOAA Atlas 14 was developed with only the 20th-century records, the NOAA Atlas 14 presents relatively uniform and monotonous changes in PFEs compared to the FSF-PM, and a systematic difference between them is identified, which we could reasonably suspect precipitation non-stationarity as the cause. It is suspected that the spatial pattern features of the NOAA Atlas result from the methodologies for mapping and filtering predicted PFE maps as described and analyzed in Kim et al. (2022).

The systematic difference is observed because of increased AMPs in the early 21st century, found by comparing the medium PRISM AMP profiles from two different time windows, 1981-2000 and

2001-2020 (not provided). The comparison presents the notable change in the medium AMP in the eastern CONUS. Considering the role of the median AMP as an index flood value in RFA, a change in PFE in the early 21st century and the difference between the NOAA Atlas and FSF-PM are reasonable.

The primary reason for the difference is the smoothing the NOAA employed. NOAA applied a dynamic filter to the precipitation frequency grids to reduce the number of station-driven PFE contours. The filter has a couple of parameters, a function of elevation gradients and proximity to the coastline. Smoothing was applied along the coast, maximum smoothing was applied in flat terrain, and the transition from one to another was gradual (Perica et al., 2018).

3.2 Climate Adjustment: Projecting Changes in Extreme Precipitation

Climate adjustment is implemented upon Pluvial Change Factor (PCF). PCF is a scaling factor to account for changes in heavy precipitation in different future periods (e.g., 2015-2030 or 2045-2060) and to adjust the baseline precipitation. Technically, PCF is a ratio of a future period's heavy precipitation expectation to a baseline period's heavy precipitation expectation, and both expectations are determined by analyzing CMIP6 GCMs rainfall projection and tropical cyclon-driven rainfall simulations.

Daily precipitation depth corresponding to a 2-yr return period is considered as the index to measure the expectations for the different time windows. The primary reason for using a 2-yr return period is to estimate a representative expectation with fewer uncertainties in estimating extreme precipitation (e.g., a 1-in-100-year event). Since GCM and TC both are projection data, we could reasonably expect that they have more uncertainty in representing future extreme precipitation. In the theory of the RFA employed for developing the FSF-PM, which is a popular approach to derive an IDF curve, a 2-yr return period is defined by the medium value (but sometimes the mean value or other percentiles) to avoid a case where a small portion of high and low values dominates the entire trend and intensify the distortion of probabilistic distribution selected to produce precipitation frequency estimates. Three time windows are regarded as representative of each climate at the period, baseline (2002-2021), current (2015-2030), and future (2045-2060).

Fig. 12 shows the workflow of creating PCFs. 18 of GCMs and 7 of TC simulation data are utilized in developing PCFs. In the representative value process, preprocessing to build an annual maximum series and deriving a 2-yr return period precipitation depth are the core processes. With daily precipitation from each GCM, the annual maximum series is built by extracting a specific percentile value for each year. For quality control purposes, the 98th percentile is selected. This is to avoid selecting an abnormally high value, which should be regarded as an outlier. Ultimately, gridded annual maximum precipitation maps for the three time periods (baseline, current, and future) are created.

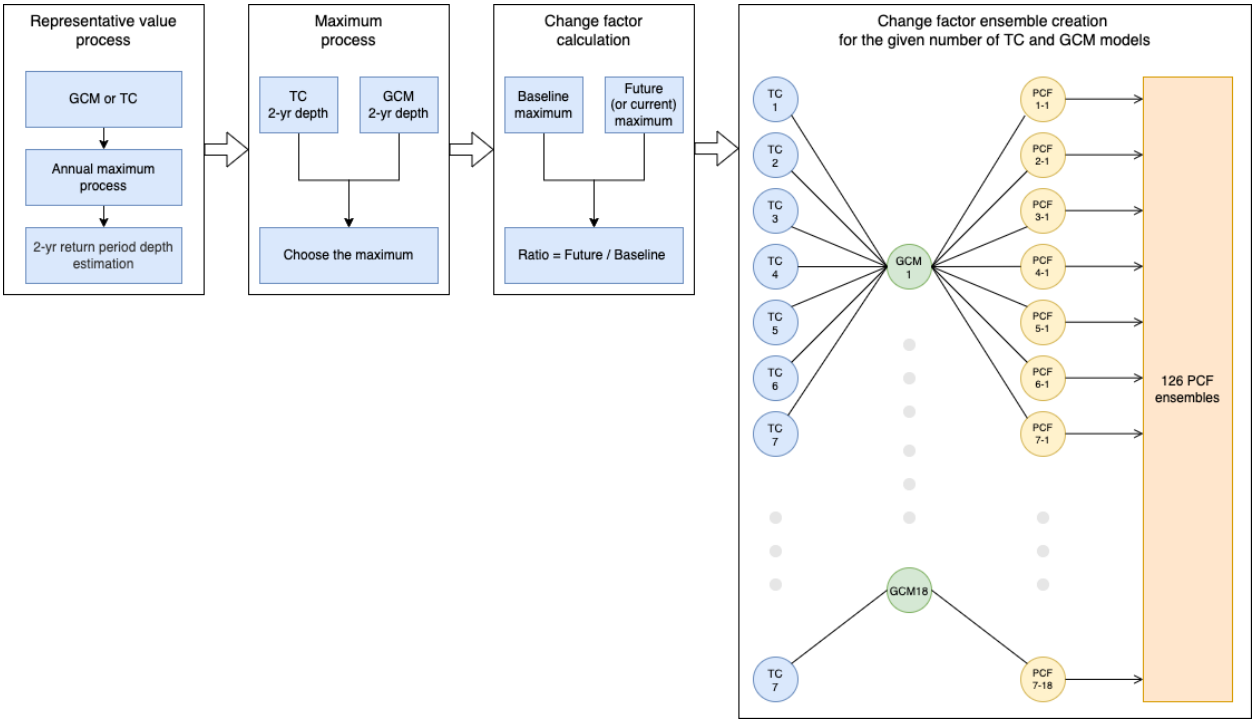

Figure 12 A workflow of the PCF ensembles creation

Annual maximum series process of the tropical cyclone-driven precipitation data is slightly different from the process with GCMs because it is built upon synthetic TC storms and sampling process. This process with the TC data requires a sampling table to build annual maximum series for synthetic years. A sampling table contains various components, such as simulation, synthetic year (season in the data), storm_of_season (order of a storm for a given year), and index number, to specify synthetic storm features. The simulation indicates an order number of tropical cyclone simulation modeling for a synthetic year.

This procedure uses large numbers of synthetic hurricane tracks derived under current (2015-2030) and future (2079-2099) CMIP6-defined climatic conditions. TC storm tracks were provided by Rhodium Group and WindRiskTech LLC and generated using methods that have been described in detail in previous peer-reviewed publications and validated well against historical observations and TC-driven rainfall generation algorithm developed by Dr. Emanuel's group is employed (Lu et al., 2018; Feldmann et al., 2019). The track generation process introduces random 'proto-cyclones' into the climate conditions of a specific GCM. These 'proto-cyclones' are allowed to move according to a Hurricane Intensity model upon which most of them die off, and the remaining events are considered the tropical cyclone climatology of a given model.

Tracks from the seven CMIP6 GCMs under SSP2-4.5 were used (Table 1). For each GCM, 50 tracks per year that made landfall along the Gulf or Atlantic Coasts with at least tropical storm intensity were generated for both the current (2015-2030) and the end-of-century (2079-2099) scenarios. To more accurately characterize the tails of the hurricane intensity distribution, an additional 25 tracks per GCM/year were generated using a higher intensity threshold. As a final layer of variance, every track was replicated into two additional ensemble members with slightly different storm characteristics, including the track path and central pressure. Combining all ensemble members results in 3,600 and 4,735 unique storms per GCM in the current/future periods, for a total universe of 58,345 unique hurricane tracks. An example subsample of a tracksuit.

A simple frequency analysis is implemented to derive rainfall depth corresponding to a 2-yr return period. The Generalized Extreme Value (GEV) distribution is selected to build a probabilistic model for each dataset, and a 2-yr return period rainfall depth is derived independently. With total 25 gridded layers of a 2-yr return period rainfall depth (18 CMIP6 GCMs and 7 TC data), 126 ensemble layers are created under the assumption that they are independent each other, as shown in Fig. 13. For example, one of PCF ensembles is created from two selected GCM and TC data (e.g., GCM#1 and TC#1).

$$PCF_{(GCM,\,TC,\,year)} = \frac{f(max\,(GCM,\,TC),\,year)}{f(max\,(GCM,TC),\,baseline\,year)}$$

Where, $PCF_{(GCM, TC, year)}$ indicates a PCF for a given GCM model, and TC simulation data, and target year (e.g., 2023 for the current and 2053 for the future). $year$ is a target year (e.g., 2023 for the current and 2053 for the future) of current or future periods (e.g., 2023 of a range of 2015-2030 and 2053 of a range of 2045-2060). $f()$ is to select a maximum 2-yr value between GCM and TC for a target year of interest. This is to account for the potential that heavy rainfalls result from localized storm events in a TC region (mostly placed along the East Coastline) and non-TC region.

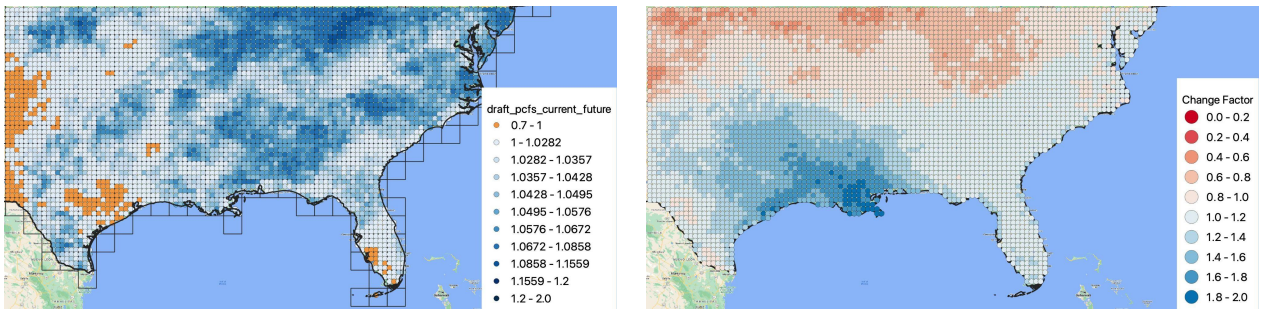

(a) GCM (b) TC

Figure 13. Comparison of the GCM-driven and TC-driven PCF distributions in the TC region: An example of specific GCM and TC models

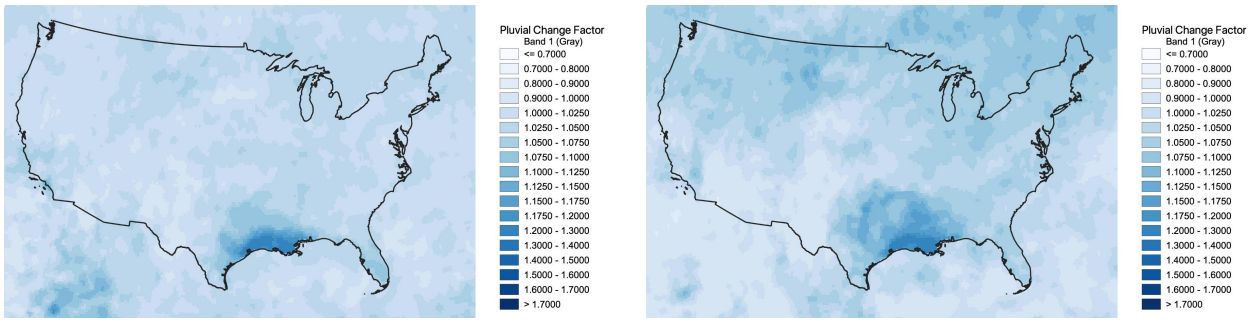

(a) Current (2023) (b) Future (2053)

Figure 14. Final PCF distributions for the current and future years

The pluvial inundation modeling uses the IDF data from the FSF-PM. These data are used to "rain-on-grid," providing precipitation inputs to the FSF-FM framework as opposed to riverine input boundary conditions. To conduct pluvial simulations under future climate scenarios, the assimilated future rainfall fields are used to derive change factors, using changes to maximum 1-day rainfall

fields for each model ensemble member. Note the assimilated future rain fields are used to produce change factors as a way of better understanding the impacts of changing environmental factors in the future. This yields distributed change factors for each ensemble member nationwide. These distributed rainfall fields are then sampled in order to provide Low, Medium and High scenarios relating to the 25th, 75th, and 75th quantiles across the ensemble members (Fig. 14). These distributed PCFs were referenced in the same way that the FSF-PM rainfall fields are currently sampled, providing three different explicit simulations of future pluvial inundation.

3.3 Pluvial Flood Modeling Execution

Pluvial flood modeling does allow for accurate discharge estimation in small channels where flooding is generally driven by intense local precipitation. For small channels (catchment area < 50 km^2), an alternative method is required, with flow generated by raining directly onto the DEM (a rain-on-grid approach). Therefore, in addition to the estimation of discharge, methods were also required for the estimation of extreme rainfall. For executing pluvial flood modeling, three processes are required to account for changes in extreme precipitation, atmosphere-land surface interaction, and changes in flood runoff in hillslopes and stream channels in a head watershed: (1) future precipitation (i.e., pluvial boundary condition) generation by adjusting baseline precipitation with PCFs (Fig. 15a) (2) infiltration modeling to simulate direct runoff (effective precipitation) (Fig. 15b, and (3) hydraulic modeling to route surface flow and simulate flood water depth by unit simulation time (Fig. 15c and d).

The rain-on-grid approach (or distributed direct precipitation) is the term used to describe the direct addition of water volume to each pixel of the model at each timestep according to the design rainfall hyetograph (i.e. simulating rainfall). An allowance for infiltration is made based on soil type using Horton's infiltration model (see section 2.3.2 for more technical details). This allowance is based on the design rainfall capacity. In the infiltration modeling, the infiltration rates (initial and terminate rates and decreasing rate) are determined by soil type and impervious area percentage, which are the parameters the model requires, and for this purpose, 30-m resolution gridded parameter layers are created and used to run the model. For accounting for the performance of stormwater drainage systems in urban and sub-urban areas, up to 20-year return period precipitation intensities are considered to represent their quantitative capacity to drain surface water out properly. As the current stormwater drainage system was built upon the national

standard, the NOAA Atlas 2 and 14 precipitation data are utilized to define their capacities depending on the level of impervious cover.

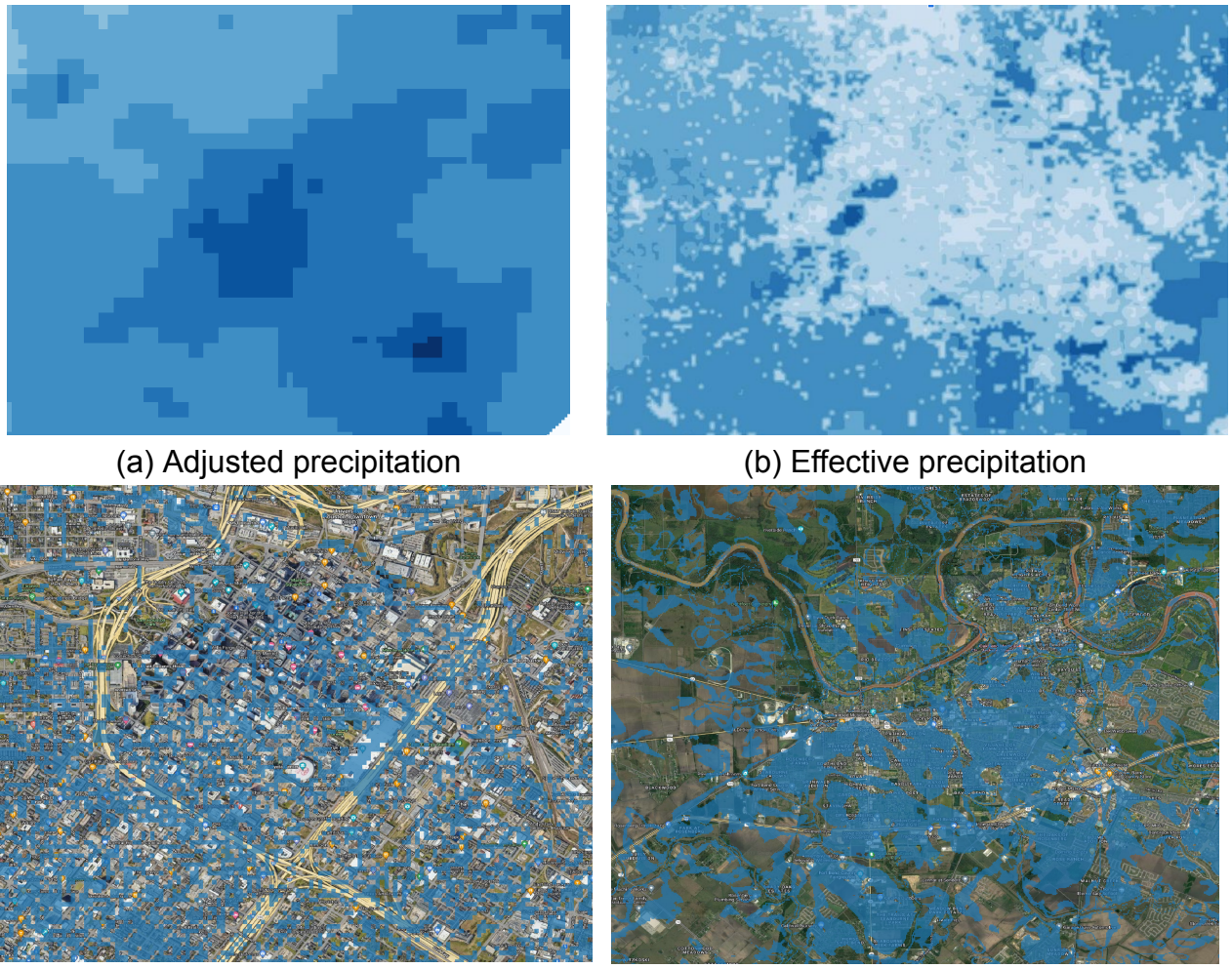

(a) Adjusted precipitation (b) Effective precipitation

(c) Urban (d) Sub-urban

Figure 15. An example (Houston, TX) of climate-adjusted precipitation and effective precipitation estimated by the infiltration model

The volumes of direct runoff at each grid are then moved across the drainage area using the shallow water equations as normal. In areas that are too steep for the shallow water equations to operate, a slope-dependent variable velocity rainfall-routing scheme is applied to move water downslope until the slope gradient decreases. The basis for this approach is predicated on the work presented by Sampson et al. (2012).

4. Fluvial Flood Risk Modeling

4.1 Regionalized Flood Frequency Analysis

In fluvial flood modeling, a regionalized flood frequency analysis (RFFA) is employed to provide lateral inflows (maybe total runoff flows combining all upper watershed inflows and lateral flows) to the hydraulic model at desired return period's flood magnitudes.

The use of direct gauge observations in order to remove the need for atmospheric and hydrological models in such instances has been used in both the academic literature and in the industry (Keef et al., 2009) as an attempt to reduce the introduction and propagation of errors from a variety of sources associated with rainfall and hydrological modeling applications. For instance, Sampson et al. (2015) highlight that precipitation data quality is a significant issue. They state that although a number of global precipitation data sets do exist, based on satellite data (Huffman et al., 2007; Joyce et al., 2004), model reanalysis (Dee et al., 2011) or gauge records (Xie et al., 2007), these products are known to have limitations that are of particular concern to flood modeling including spatially variable biases (Kidd et al., 2012), poor correlation with ground gauges at short (~daily) time scales (Chen et al., 2014; Cohen Liechti et al., 2012), poor representation of spatial variability over smaller catchments (He et al., 2009) and a tendency to underestimate heavy rainfall (Chen et al., 2014; Gao and Liu, 2013). Sampson et al. (2014) evaluated the effect of these differences on flood risk using a cascade model structure that replicates an insurance catastrophe model and found estimates of monetary loss from flooding to vary by more than an order of magnitude depending on whether the cascade was driven with gauge, radar, satellite, or reanalysis data. Similarly, it is well known that extreme flows in ungauged catchments remain a key challenge to the field of hydrology (Bloschl et al., 2013).

The probabilistic discharge estimates used by FSF-FM are based upon direct observations of streamflows, linking extreme flow behavior in gauged catchments to estimate what gauged observations would likely be in ungauged catchments. This process involves taking streamflow information from gauged catchments and applying those to ungauged catchments that are similar in nature to the gauged catchments using a series of indicators related to grouping catchments based on a set of predetermined characteristics.

The main forcing required by the FSF-FM is a set of inflow boundary conditions derived from RFFA (Smith et al., 2015). The RFFA utilizes a hybrid-clustering approach in conjunction with a flood-index methodology. The methodology used here is similar to that employed by Smith et al. (2015); however, it has been updated owing to the far denser network of gauges in the U.S. in comparison to global RFFA. The method employed consists of two steps: firstly the estimation of an index flood is undertaken, followed by the scaling of this index-flood using growth curves that describe the relationship between the index flood and extreme flow magnitudes. The index flood used here is the mean annual flood, with the method used to define the mean annual flood differing from that employed by Smith et al. (2015). To best utilize the far denser USGS gauge network, gauges were partitioned in space to estimate the index flood. Therefore only gauges from the same river or hydrological zone were used in the estimation of the index-flood. However, for the estimation of the growth curves, gauges were pooled together across all catchment zones—this was undertaken to avoid temporal sampling errors.

For the first stage of this procedure, the estimation of the index or scaling flood, gauges are partitioned in space, using both a river identification number and the USGS Hydrologic Unit Code (HUC) data to place gauges into their respective hydrological groups. The HUC boundaries for HUC 2 (Regions), HUC 4 (Subregions), HUC 6 (Basin), HUC 8 (Subbasins), HUC 10 (Watersheds), HUC 12 (Subwatersheds), HUC 14, and HUC 16. The method used here to estimate the mean annual flood uses a hierarchical system to link observed mean annual flood estimates to upstream areas for individual rivers and HUC zones. The method proceeds as follows: firstly, for individual river reaches, the procedure checks whether there are a sufficient number of gauges and a sufficient number of gauge years present. It also checks whether a sufficient sample of the individual river is available; this is defined by checking whether minimum and maximum area thresholds are satisfied. The gauge number, gauge record length, and minimum and maximum area thresholds are pre-defined parameters that when met allow for power laws to be fitted between upstream areas and discharge/index-flood. For gauges on an individual river, when sufficient record lengths and gauges are present, and the river is adequately sampled when it is both small and large, individual power laws are stored to estimate discharge across any part of the river.

For other rivers that do not have either sufficient gauge coverage or sufficient coverage in space, gauges are pooled together with gauges from other rivers according to their respective HUC zones.

The procedure then uses a hierarchical system moving from small HUC zones to large HUC zones, checking whether the same threshold parameters described above are satisfied. When the threshold parameters are met for an individual HUC zone, the relationship between the upstream area and discharge/index-flood is defined again using a power law. If the parameters are not met, the procedure moves up to the next level HUC zone, pulling in more gauges, with the procedure continuing until the parameters are satisfied.

For the second part of the RFFA procedure, the methodology uses the growth-curve procedure outlined by Smith et al. (2015). As discussed above, the method does not partition gauges in space in an attempt to limit temporal sampling errors. Instead, the method uses catchment descriptors of climate class, upstream annual rainfall, and catchment area and proceeds as follows: data from available river gauging stations are subdivided into the five main categories of the Koppen-Geiger climate classification (Kottek et al., 2006), as shown in Fig. 16. A clustering method is then used to pool together suitably homogenous catchments; the clustering method used for regionalization is a combination of Ward's algorithm and k-means clustering (Ramachandra Rao and Srinivas, 2006). Extreme value distributions or flood frequency curves are then fitted to each of the pooled groups, providing relationships between the index-flood described above and extreme flows for any recurrence interval, for each of the pooled regions. When combined with the index flood, MAF, the flood frequency curves or growth curves provide a basic means of flood estimation for any region (Meigh et al., 1997; Zaman et al, 2012).

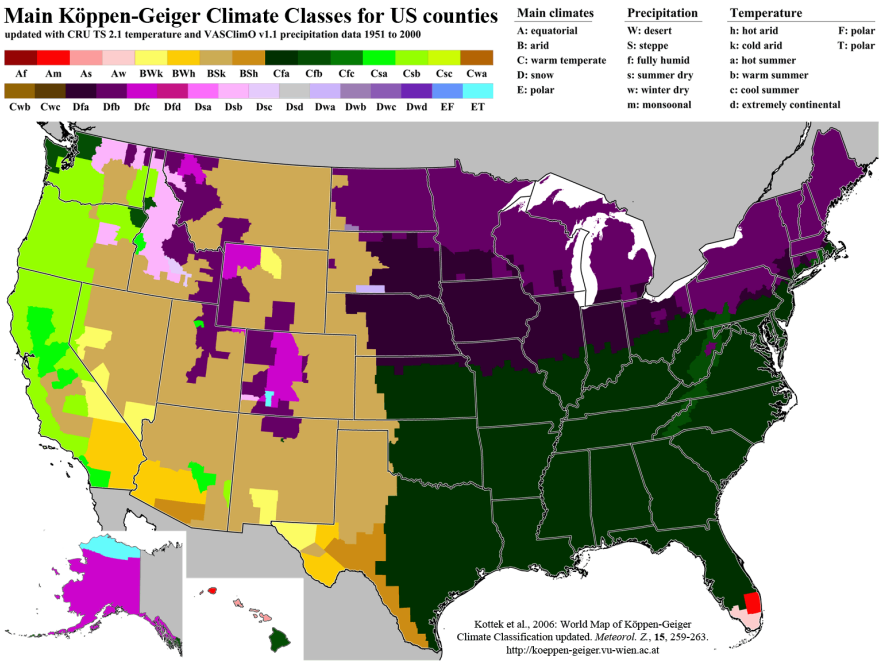

Figure 16. Koeppen-Geiger climate zones across the Contiguous U.S. (Source: http://koeppen-geiger.vu-wien.ac.at/usa.htm).

Smith et al. (2015) applied these methods to a global data set of over 3,000 gauging stations, sourced from the Global Runoff Data Centre (GRDC) and from the USGS stream gauge network (http://nwis.waterdata.usgs.gov/nwis). Although the ability of this approach to provide detailed, localized discharge estimates is limited by the simplicity of the methods, significant uncertainties in the discharge record, and the complexity of anthropogenically modified river systems, these methods have demonstrated skill in providing first-order discharge estimates in data-poor regions (Padi et al., 2011; Smith et al., 2015). Estimating extreme discharge via this method is subject to significant uncertainty, as is the case with all generalized global methods; although global mean errors of ~80% were reported by Smith et al. (2015), far larger errors were also reported, in some cases >300%. Even though the errors in estimating flow in the U.S. are anticipated to be far lower, due to far denser gauging/sampling, significant errors will still exist. Because such errors are currently unavoidable in large-scale discharge estimation, discharge estimation bias is explicitly accounted for in the modeling framework by scaling channel conveyance within the hydraulic model according to the estimated bankfull discharge.

Design discharges for ten different recurrence intervals (5, 20, 100, 200, and 500-year) were

calculated for all river reaches utilizing the methods detailed above. In reference to the relationship between recurrence intervals longer than the span of the historically observed data, the RFFA method pools together catchments/gauges into homogenous groups. Growth curves are then derived from these groups by normalizing the extreme values for each gauge by their mean annual flow. Therefore, instead of the absolute discharge values, the extreme values for each gauge are a function of Discharge/Mean Annual Flow. Each pooled growth curve typically contains hundreds of years of data.

4.2 Fluvial Flood Risk Projection

Framework

For the future inland fluvial simulations, outputs from GCMs will be used to generate estimates of current and future discharge time series, from which discharge Fluvial Change Factors (FCF) will be generated. Fig. 17 shows the core processes and workflow to create fluvial change factors for projecting future fluvial flood risk. An ensemble of climate models will be driven through a set of representative, calibrated, rainfall-runoff models. The run-off model used will be HBV, a lumped hydrological model that has been widely used in climate impact studies. The assumption used in having representative catchments is the same used in regionalized flood frequency analysis; data for catchments in gauged/sampled areas can be linked to ungauged catchments using a set of catchment descriptors. Following the simulation of current and future time-series through the calibrated run-off models, a set of FCFs will be generated between the current and future estimates of discharge. These FCFs will be linked to the catchment characteristics from which they were generated, allowing them to be mapped onto the FSF-FM modeling framework.

With a set of rainfall-runoff models being calibrated across representative catchments, the next stage is to drive the model set with output from a climate model ensemble. The model ensemble used the daily downscaled CMIP6 projections, which are GCMs that have been bias-corrected and downscaled across the U.S. Each of the models in the ensemble will be driven through each of the calibrated HBV models for both current and future climates.

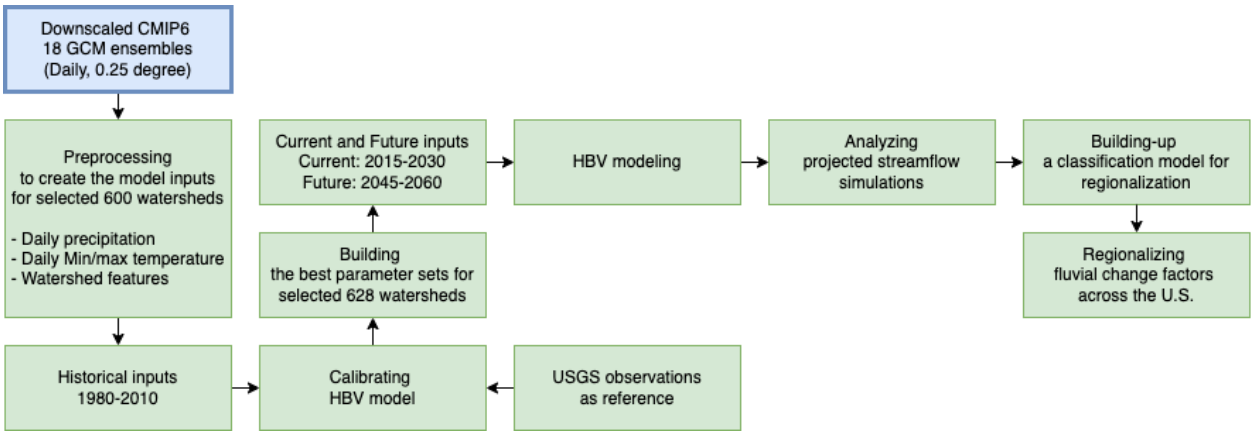

Figure 17. A workflow of creating fluvial change factors

The total 628 catchments being simulated to derive FCFs depends on computational resources and time. This will yield 18 representations of current discharge and 18 representations of future discharge, one for each model in the ensemble. To derive FCFs for all individual river reaches in the United States, a classification model was built upon the selected catchments by considering their climatic and hydrologic features such as annual precipitation, drainage size, and climate zone. The decision taken here was to use a regionalization method, whereby we use a pool of calibrated models and assume that they are representative of other similar catchments. We filled out this sampling pool with more catchments, and generated FCFs for ungauged river reaches.

HBV modeling in fluvial flood risk projection

To update the model framework detailed above, and in order to account for climatological changes that have occurred over the duration of the USGS and NOAA-derived observational boundary conditions, a climate model ensemble will be used, in conjunction with synthetic hurricane tracks and precipitation. The process used here will be to run an “observed” and a “current” climatology through a set of representative rainfall-runoff models across the U.S. This is done in an effort to update the observed climatology that the current FSF-FM hydrologic model uses. The “observed” time period will be the 1980-2010 period and the “current” will be the 2015-2030 period. The process used here will be to extract the data for these time periods from an ensemble of 18 GCMS, run them through the HBV catchments discussed in more detail in the subsequent sections, and then produce flow frequency curves for both the observed and the current climatologies. The differences between these flow frequency curves, for each of the model ensemble members and

each of the sample HBV catchments, will then be used to perturb the existing hydrologic model.

Hydrological modeling within selected catchments

Inferring change factors of discharges between current and future scenarios in as many places as possible requires a robust regionalization approach, which in turn needs a representative selection of various catchment characteristics, including historical discharge time-series simulated using a well-calibrated hydrological model. For this purpose, HBV is used to simulate daily streamflow time-series from climate projection weather variables such as temperature and precipitation.

A total of 628 watersheds representing rivers/tributaries of various sizes and discharge magnitudes were selected across nine different Koeppen-Geiger climate zones (Fig. 11), including 23 representative coastal basins. For most basins, a record of observed discharges of at least 30 years was available and used for the calibration of a lumped HBV hydrological model. The hydrological model is not being used to simulate floods everywhere. A regionalized flood frequency analysis is used to derive the input flows for the hydraulic model framework. The run-off modeling undertaken here is used to derive perturbation factors for the existing hydrologic model. The absolute discharge values coming out of the calibrated run-off models, which would undoubtedly be subject to significant uncertainty, are not used. We instead only use the relative changes between simulated time horizons.

Since each basin behaves differently, calibration was performed separately for each. For each basin, a set of model parameter values were generated randomly around the closest validated parameter set provided by Beck et al. (2016), and 2000 realizations of HBV models were performed. This produced a range of discharge time series for each basin. 63% of the basins included the observed discharge within their simulated range for more than 90% of the time over the total observed record length, with an average of 86% across all selected basins (Figure 5). In almost all cases, HBV simulated the expected discharge within an acceptable range (Beven, 2006) on an average 11,600 days out of 13,500 days. Unsurprisingly, lower performance was generally observed in flashy basins in semi-arid climates and in snowmelt-dominated high-latitude basins. There was no notable difference between the coastal and inland basins simulated. Additionally, separating out high-flow periods for assessing the model did not significantly change performance.

For simulating current and future change scenarios using the CMIP6 GCMs, the best-performing HBV model was selected for each basin. As an important consideration, uncertainty in the run-off modeling component of the model cascade isn't being undertaken. Instead, we selected the best-performing HBV model based on its performance under the current climate conditions. Future iterations of this process will take the time to better account for uncertainty in the current climate and potential alignment with future projections. However, to account for the likely situation of an acceptable model parameter set not performing well in future climates, we first looked for behavioral model parameter sets in the two thousand simulations for each basin using gauged discharge records. Given that we're unable to explore uncertainty in the hydrological modeling component, an assumption here is that models performing well under the current climate will perform in a satisfactory manner under future climate scenarios. This procedure focused on only retaining those model parameter sets of the behavioral sets that perform best above the 99% percentile, so it is focused on high flows. Additionally, A Kendall trend test is used to uncover temporal trends in the data. Gauge records with significant trends have not been included in this analysis (after Quinn et al 2019). Further tests search for sudden shifts in the record time series (e.g. due to gauge movement), and again, records are removed if they fail this test.

Regionalization of change factors

The FSF-FM framework simulates inundation for every single river in the U.S., regardless of size. To allow a commensurate, comprehensive simulation of future flows across all rivers, estimates of future discharge also need to be generated for all rivers. Although extensive, existing gauge networks in the U.S. do not cover all rivers. Therefore, the methodology used here is similar to that used to generate flows for all rivers; potential changes to extreme flows will be linked to catchment characteristics. These characteristics can be generated for every single river in the U.S. and are the same as those used in the existing FSF-FM hydrologic model. As a result, the change factors generated for each of the representative catchments can be mapped onto the existing framework using these catchment variables.

4.3 Fluvial Flood Modeling Execution

The FSF-FM defines upstream catchment characteristics for each of the model input boundary conditions. These same catchment characteristics are used to define perturbations of future flooding for each of the simulated recurrence intervals. Therefore, the FSF-FM was executed in the same way as outlined above, with the addition of a perturbation step referencing the catalog of change factors as described in the preceding section. FCFs provide a range of different change factors for each recurrence interval. To sample across this range, Low, Medium, and High scenarios are simulated relating to the 25th, 50th, and 75th quantiles across the ensemble range for each of the representative catchments. Therefore, for each simulated recurrence interval, three separate model realizations are undertaken.

5. Coastal Flood Risk Modeling

5.1 Framework and Data Sources

In order to produce climate-adjusted current and projected coastal flood risks, the FSF-FM operates by ingesting coastal water level boundary conditions. These boundary conditions are generated from normalized time series and return period curves, which span across the entire East, Gulf, and West Coasts. NOAA gauge stations provide authoritative water levels and tide data for the US, but they are spatially limited. Additionally, water levels are greatly affected by waves, along with potential storm surges and sea level changes. The coastal model captures these ingredients separately for the East and West Coasts, while the Gulf Coast is combined with the East Coast. Fig. 18 illustrates the overall coastal processing workflow. This section details each of these components, and the following sections describe the process for obtaining the boundary conditions on each coast.

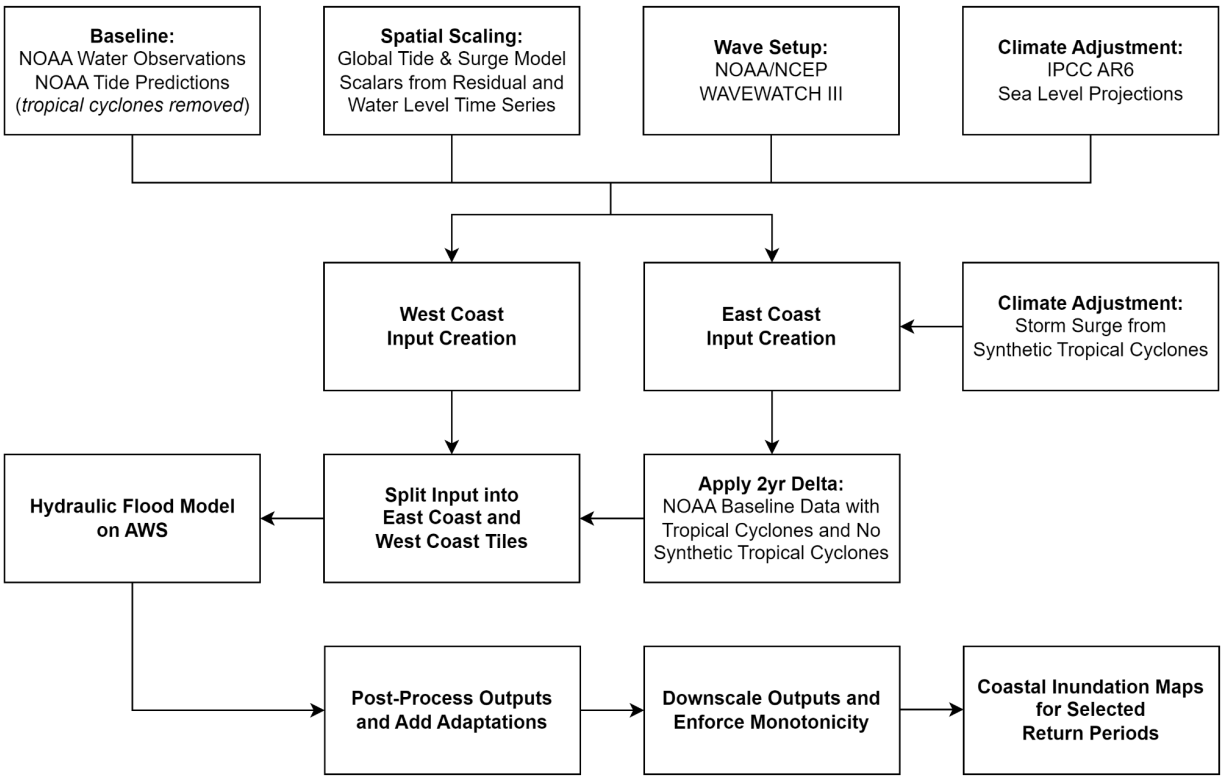

Figure 18. A workflow of the U.S. coastal modeling

5.1.1 Baseline: NOAA Water Level Observations and Tide Predictions

The coastal portion of the FSF-FM uses NOAA's daily maximum and minimum water level observations and tide predictions from 01-Jan-1950 to 31-Dec-2018. Data from all of NOAA's gauge stations were considered (https://tidesandcurrents.noaa.gov/) and then restricted to those with a minimum of 25 years worth of data, with each year consisting of at least 80% of each year (Fig. 19). This culminated to 67 stations along the East, Gulf, and West Coasts.

NOAA generates the tide predictions from harmonic and tidal analysis (Parker, 2007), which involves a mathematical calculation of the expected tidal conditions created by the relative motions/positions of the Moon, Sun, and Earth (Ehret, pers. comm., October 17, 2022). This calculation is run on-demand at the time the prediction is requested. Unlike the water level observations, there is no tidal data inventory or database. All of these water levels were detrended for mean sea level change over time to match the 1983-2001 National Tidal Datum Epoch (www.tidesandcurrents.noaa.gov/datum-updates/ntde/). This dataset serves as the baseline and main coastal boundary conditions from which all other boundary conditions center around.

Figure 19. A map of the NOAA gauge network

5.1.2 Spatial Scaling: Global Tide and Surge Model

Since the NOAA data is spatially limited, additional data is needed to cover the coastlines between these stations. The Global Tide and Surge Model (GTSM) is typically used to model water levels and currents, but instead, the FSF-FM uses GTSM locations to interpolate along the coastline and fill the gaps between NOAA's gauge stations. While raw values are not used in the model, a ratio of the 99th percentile daily maximum (Q99) levels is extracted from these locations to observe the relative change over a 30-year range along with the residuals. There are 1,431 GTSM locations on the East and Gulf Coasts and 251 on the West Coast.

The FSF-FM finds the GTSM location closest to each individual NOAA gauge station. These locations become pseudo-stations representing their neighboring NOAA station. All remaining GTSM locations are then linked to their nearest representative GTSM location. Spatial scalars are created from the ratio of the GTSM Q99 and their representative GTSM location Q99. Then these values are used as a multiplicative factor to scale across the coastlines between NOAA gauge stations. This produces boundary conditions along the entire coast, expanding beyond the locations of the 67 NOAA stations.

5.1.3 Wave Setup: WAVEWATCH III

Waves are another major contribution to water levels. Wave setup is the mean water level at the shoreline due to waves breaking. To capture these phenomena, the FSF-FM uses daily wave hindcast time series from WAVEWATCH III (WWW3). The time series range from 1979 to 2009 (polar.ncep.noaa.gov/waves/hindcasts/). The distribution of wave conditions is developed by matching the WWW3 time series to the nearest coastal boundary conditions. Wave hindcasts that do not overlap with the dates from the GTSM data are removed, along with values that exceed the 95th percentile maximum. Wave setup is traditionally calculated as twenty percent of the offshore significant wave height (www.coastalwiki.org/wiki/Definitions_of_coastal_terms). The FSF-FM uses this value, and wave-protected areas use an additional multiplicative factor to dampen the value. Since these areas all have unique geographical features, they are each carefully assigned a value customized for each location.

5.1.4 Climate Adjustment: Sea Level Projections and Storm Surge

The two other major contributors to coastal water levels are sea level change and hurricane storm surge. Factoring in these components uniquely allows the FSF-FM to be climate adjusted. Most importantly, it contributes to the main goal of V3, which was to upgrade the model by incorporating CMIP6 outputs. The CMIP6 outputs were used to develop the sea level projections and storm surge data incorporated in the FSF-FM (see Sections 2.2.2 and 2.2.3).

Sea level change factors are calculated using the AR6 sea level projections at each NOAA station. These values are critical for determining mean sea level change factors and future water levels. The surge data is sampled along with the GTSM and wave data to produce the coastal boundary conditions necessary to run the model. The following sections detail how this is done.

5.2 West Coast

The sole purpose of pre-processing is to establish coastal boundary conditions for the model. Since there is not enough NOAA data to cover the entire coastline, GTSM data is used to scale the available NOAA data along the entire coast with waves added. This is the process used to develop boundary conditions along the West Coast. The West Coast begins with data from 19 NOAA stations and expands to 9,608 boundary conditions.

The process begins by calculating the mean sea level change factor (CF_{MSL}). The NOAA data from 1980 to 2015 is fit to a third degree polynomial to predict the mean sea level of 1992 (MSL_{1992}), the tidal epoch's central year, and 2020 (MSL_{2020}), the historical baseline year. Subtracting them yields the mean sea level change factor from 1992 to 2020:

$$CF_{MSL} = MSL_{2020} - MSL_{1992}$$

Similarly, the IPCC AR6 sea level projections from 2023 (SLR_{2023}) and 2020 (SLR_{2020}) are subtracted to calculate the sea level change factor, CF_{SLR}:

$$CF_{SLR} = SLR_{2023} - SLR_{2020}$$

The year 2023 represents the current year of the FSF-FM. These change factors are produced to ultimately find 1992 to 2023 mean sea level change factor (CF_{2023}), which is calculated by adding them:

$$CF_{2023} = CF_{SLR} + CF_{MSL}$$

These calculations occur at each NOAA gauge station and corresponding PSMSL gauge station. See Table 5 for 1992 to 2023 mean sea level change factors for the West Coast. Obtaining the change factors at these stations will allow water levels to be interpolated along the rest of the West Coast.

A piecewise distribution with Pareto tails is estimated from the daily NOAA tide peaks. At each NOAA station, 5,000 years of synthetic events are generated based on this distribution. A random tide is assigned to each event and updated with the mean sea level change factor, CF_{2023}. These time series are subsequently scaled at each GTSM location by multiplying the time series and their associated spatial scalar. This Monte Carlo approach produces synthetic water levels at every GTSM location scaled from NOAA station data. These GTSM locations must be matched to the 9,608 locations from the coastal boundary file. This is simply done by finding the minimum distance between the locations using the Pythagorean Theorem.

Wave setup is added first by sampling from a distribution with Pareto tails of the significant wave heights which exceed the 95th percentile daily maximum (Q95) values. Then 20% of the significant wave heights are used for wave setup. Last, the wave setup is added to the water levels at the coastal boundary locations, and return period curves are calculated. Finally, water levels with wave setup are available at each location along the West Coast. Additionally, normalized time series are calculated at each location by using the mean of the hourly NOAA Q99 peaks. This accounts for the 2023 median coastal boundary conditions.

The remaining low, median, and high scenarios for 2023 and 2053 are derived from this data and sea level projections. The return period curves for these files are generated by creating change factors from their corresponding sea level projections and adding this change factor to the 2023 median results.

Table 5. 1992-2023 Mean sea level change factors for the West Coast

NOAA ID	Lat	Lon	PSMSL ID	Lat	Lon	$CF_{2023}(m)$
9410170	32.70222	-117.168	379	-117.158	32.68229	0.093
9410230	32.86667	-117.251	192	-117.246	32.87621	0.077
9410660	33.71722	-118.268	217	-118.271	33.72396	0.074
9412110	35.16694	-120.751	323	-120.762	35.18229	0.067
9413450	36.60083	-121.884	260	-121.934	36.61458	0.072
9414290	37.80111	-122.453	4927	-122.49	37.78646	0.071
9414750	37.7675	-122.300	4911	-122.314	37.78646	0.044
9415020	37.98556	-122.968	4927	-122.49	37.78646	0.079
9416841	38.9025	-123.702	17	-123.691	38.90625	0.045
9418767	40.76667	-124.217	150	-124.248	40.75521	0.138
9419750	41.73528	-124.184	82	-124.16	41.74479	-0.010
9431647	42.73417	-124.486	322	-124.482	42.73438	0.006
9432780	43.33528	-124.318	4886	-124.248	43.46354	0.044
9435380	44.61806	-124.035	409	-124.043	44.63542	0.072
9439040	46.20111	-123.767	21	-123.926	46.22396	0.050
9440910	46.70139	-123.967	438	-124.072	46.69271	-0.011
9443090	48.36722	-124.600	275	-124.629	48.38542	-0.031
9444090	48.11806	-123.435	313	-123.457	48.15104	0.023
9447130	47.60028	-122.334	4862	-122.373	47.57813	0.070

The 2023 low change factor (CF_{Low}) is created by subtracting the median quantile sea level projection (SSP 245 quantile 0.50) from the lower quantile sea level projection (SSP 245 quantile 0.167):

$$CF_{Low} = SLR_{0.167} - SLR_{0.5}$$

Similarly, the 2023 high change factor (CF_{High}) is created by subtracting the median quantile sea level projection from the upper quantile sea level projection (SSP 245 quantile 0.833):

$$CF_{High} = SLR_{0.833} - SLR_{0.5}$$

The 2023 high (2023_{High}) and low (2023_{Low}) exceedance probability scaled return period curves are produced by adding these change factors to the 2023 return period curves (2023_{Median}):

$$2023_{High} = 2023_{Median} + CF_{High}$$

$$2023_{Low} = 2023_{Median} + CF_{Low}$$

The same methodology is used to produce the 2053 low, median, and high return period curves. Change factors are developed by subtracting the 2023 median sea level projection from each future sea level projection scenario. Then the results are added to the 2023 median return period curves to produce return period magnitudes for these future scenarios.

5.3 East Coast

The East and Gulf Coasts (herein East Coast) are modeled separately to include storm surges. The process is similar to that described in Section 5.2, but the East Coast uses the 24,018 synthetic tropical cyclone output coordinates as the boundary locations. Since there are only 48 NOAA gauge stations on the East Coast, GTSM spatial scalars are used again to interpolate along the coastline, but the water levels must be merged with the surge data.

The process of combining water levels with storm surge events from the synthetic tropical cyclone tracks is done by looping water levels at each coastal point with surge data from each model (CESM2, EC-Earth3, NorESM2, UKMO6, MIROC6, MPI6, and MRI6). Return period curves are produced by adding the appropriate change factors with a ranking method. The current synthetic tropical cyclone dataset spans from 2015 to 2030. Future return period curves are calculated using the same process with the 2045 to 2060 synthetic tropical cyclone dataset and future sea level rise projections. The 25th and 75th percentiles calculated from the median ensemble of return period curves are used with the future sea level projections to calculate the remaining 2023 and 2053 low, median, and high time series.

In some areas, mostly southern Florida, an unusually large frequency of synthetic tropical cyclones results in unrealistic storm surge levels. To remedy this problem, a two-year delta is applied to the inputs before they are supplied to the model. This delta is calculated and applied in three steps. Previously, the water levels at each coastal point were calculated with historical tropical cyclone data removed in order to avoid double counting with the synthetic tropical cyclones. The first step recalculates the water levels with historical tropical cyclones and no synthetic tropical cyclones. The second step recalculates the return period curves in the same manner with no synthetic cyclones. Finally, zero, one, and two-year deltas are calculated, but only the two-year delta is applied to this data with the results smoothed of any outliers. This completes the coastal boundary file creation, holding scaled return period curves and normalized time series.

The scaled return period curves and normalized time series are the basis for creating the time-varying channel and floodplain boundary conditions necessary for the coastal model. An associated sub-grid channel network, including channel bank heights, bed elevations, widths, locations, and directions, is also critical to the model. Most importantly, the model can only be as accurate as the digital elevation model available.

5.4 Coastal Flood Modeling Execution

The scaled return period curves and normalized time series are the basis for creating the time-varying channel and floodplain boundary conditions necessary for the coastal model. An associated sub-grid channel network, including channel bank heights, bed elevations, widths, locations, and directions, is also critical to the model. Most importantly, the model can only be as accurate as the digital elevation model available. Each of these components are discretized into current and future Low, Medium, and High scenarios with associated 25th, 50th, and 75th quantiles based on the scaled return period curves and normalized time series. This ensemble of model inputs originated from the mean sea level and sea level change factors detailed in Section 5.2.

6. Discussion

Summary

The sections above outline the development of FSF-FM V3 that encompasses inland and coastal flooding risk into a single comprehensive model. Both the inland and coastal models are created to account for climate uncertainty current (2023) and into the future (2053) in the unique ways that climate will impact risk as a non-stationary process. The inland models are developed using LISFLOOD-FP and national scale fluvial/pluvial risk modeling components with the added refinements of being downscaled to a higher resolution in order to facilitate the development of risk profiles for every property in the non-coastal U.S. Likewise, coastal risk models are developed using GEOCLAW, with significant alignment and calibration checks in comparison to ADCIRC, and downscaled to the same high resolution as the inland models in order to produce the same flooding risk profile at the property level. The coastal models are further coupled with localized tidal water levels and the same fluvial/pluvial models developed for the inland risk models to allow for a full range of risks to be accounted for in the more complex coastal regions of the country.

The high-resolution hazard layers in both the inland and coastal contexts are reviewed and refined across multiple iterations to account for issues associated with discontinuity, overly aggressive flooding extents, the absence of flooding in areas with flooding reports/FEMA claims, and missing adaptation infrastructure. The resulting hazard layers are then trained in order to understand their relationship across return periods within the current year state (2023) in order to interpolate missing periods and then trained across future years using a strategic set of explicitly modeled hazards through 2053. The resulting set of high-resolution interpolated hazards allows for the production of cumulative statistics at a property level for selected flooding depths, across selected return periods, for every property in the U.S.

Limitations

Uncertainties of hydraulic-hydrologic modeling and data

There are a number of known limitations that must be understood in the interpretation and use of the FSF-FM. Those limitations relate primarily to the original resolution of the hydraulic and hydrodynamic flood models as well as the introduction of climate uncertainty into the larger risk modeling scheme. The limitations are not unknown to risk modelers, and the methods outlined in the document above actually reduce the impact of these limitations significantly when accounting for the scope of the model. That being said, these limitations should be understood in order to evaluate the utility of the model for any single purpose.

Even though there are thousands of usable river gauges in the U.S., there are still ungauged catchments that require estimation methods for flow. In these areas, it is more likely hazard layers will under or over-represent flood risk. This limitation is similar to the sparsity of gauges along the coasts that measure water levels, which is particularly more important for estuaries like tidal water bodies that are behind barrier islands. The tidal harmonics in these locations are less likely to be accurately represented, and it is harder in these areas to validate and calibrate storm surge model behavior.

Since the hydraulic modeling is executed at 30-meter horizontal resolution using a 30-meter DEM, it is possible that smaller elevation features affecting the flow of water may be missed. A series of GIS steps using higher resolution elevation datasets (1-3 meters) attempts to identify any elevation feature that can impede flow, which leads to either DEM updates or identification of areas protected by adaptation, however, some areas are likely to be missed.

The exact climate response to already emitted greenhouse gases is unknown, and therefore possible sea level, hurricane intensity, hurricane precipitation, non-hurricane precipitation, and stream discharge projected changes will deviate from reality. In addition, the choice of CMIP6 SSP2-4.5 assumes a concentration pathway with no guarantee of occurring. By creating hazard layers reflective of both the high and low ends of the climate models, some uncertainty is being communicated, but it is possible some climate responses will end up outside the modeled extremes.

A key component of flooding modeling is accurate elevation inputs, and due to the nature of elevation projects, some areas have older, less accurate DEMs. In these areas, the hazard layers are more likely to miss the impact of recent development or key elevation features than can impact hydraulic modeling.

The “increased infiltration rate” mechanism used to incorporate green infrastructure into the flood models is a simplified approximation for how these types of structures reduce flooding. The flood reduction capabilities of green infrastructure projects are far more nuanced than this simple mechanism, but this method does offer a simple and consistent solution to account for the increased infiltration rates offered by the pervious surfaces associated with these types of structures.

Uncertainties of tropical cycolne modeling

The adaptation mesh utilized in GeoClaw is computationally efficient. However, if the mesh resolution is too low in key areas, water behavior is likely to be mischaracterized. This is particularly true in narrower water bodies such as canals. Therefore, water level estimates in these locations can deviate from what would be obtained if a higher-resolution mesh were used to propagate water through narrow passageways.

While evidence from the atmospheric sciences literature indicates that warmer sea surface temperatures will drive the potential for larger, wetter, more powerful, slower-moving, and thus more damaging storms, actual extreme storms are rare events, especially on a location-by-location basis. This makes studying future tropical cyclone activity and associated losses highly uncertain, as the risks are driven by tail behavior.

We rely on the simulated climates from GCMs to represent the changes in tropical cyclone behavior, including those of extreme events. Across our broad set of simulations, each model simulates ocean currents, jet streams, ENSO, etc., and has behavior that includes random variability along with the climate change signal. This variability, combined with the broader climate change signal, creates tail events in the model. However, this also means that projections of tropical cyclone activity can be particularly noisy. Even after simulating hundreds of thousands of synthetic tropical cyclones, we can see counterintuitive patterns, particularly on a local scale. This

is helpful to keep in mind when reviewing the tropical cyclone impacts from the model.
The complex range of phenomena that impact tropical cyclone activity makes modeling changes in that activity due to climate change quite challenging. We, therefore, take an approach that focuses on capturing the long-term trend during the 21st century rather than prescribing activity at specific dates throughout the 21st century.

To capture the effect of changing hurricane activity on flood risk, we use a surge model (GeoCLAW), which efficiently simulates TC-related storm surges to simulate a very large library of storms. The computational efficiency of this model allows us to cover a range of GCM climatologies, scenarios, and periods, but we do sacrifice some elements of realism which might be used in a more detailed study of flood risk. Specifically, we assume that sea level rise, storm surge, and wind-based wave runup may be combined linearly. In reality, these drivers of flood risk interact with each other and the bathymetry and surfaces they flow over. We feel that, for the purposes of characterizing changing drivers of risk due to climate change, the downsides of this approach are small and are outweighed by the ability to model a very large simulation library, using a diversity of modeled sea level rise and climate states as storm behavior drivers.

Surge effects were not included on the Great Lakes or other large, non-ocean water bodies. This is a model feature in development that will be added in a future version.

Uncertainties of adaptations

The existence and operation of flood control structures and adaptation measures can significantly impact flooding and, therefore, model results. The FSF-FM attempts to account for these measures as much as possible. However, several limitations should be acknowledged for the adaptation data used in modeled flood layers.

Service areas were sometimes digitized manually when the spatial extents of an adaptation structure's service area couldn’t be found in the available documentation. This was done at the location of the adaptation structure by overlaying the internally modeled flooding extents of the return period year that matches the return period for which the structure was designed. This procedure was used to estimate where flooding should logically be removed but is in no way an exact science.

Flood risk related to an adaptation project's structural integrity was not accounted for. Structures were universally assumed to protect for all flood events up to the documented return period level of protection they were designed for, regardless of structure age, risk of degradation, lack of maintenance, etc. This notably includes dams and levees, where the FSF-FM does not quantify the risk of failure.

A few comprehensive adaptation databases exist at the municipal/county level, and no known comprehensive datasets exist at the state or national level. The development of a comprehensive national adaptation dataset for use within our flood models required a level of effort greater than what could be produced by the five team members tasked with this objective. In the interest of time and efficiency, geographic research areas for adaptation data collection were prioritized. A research approach was therefore developed, limiting areas of investigation to the 10 most populous counties in each state.

Hot Models

The lastest CMIP6 generation of climate models includes a subset of hot models that point towards much greater warming than expected (https://www.carbonbrief.org/guest-post-how-climate-scientists-should-handle-hot-models/). In the FSF-FM development, 7 hot models (according to TCR screen 'Likely' criteria) are used among 18 GCMs (Table 6). As described in the methodology section, GCMs are used in creating climate adjustment factors for fluvial and pluvial flood modeling. To understand their effects on the FSF-FM performance, we validated their effects on change factor creation by grouping the hot models and non-hot models. As a result, notable differences have not been found in the analysis. We suspect this is because a change factor is a ratio of two representative values (e.g., 2-year extreme precipitation of 2015-2030 / 2-year extreme precipitation of 2045-2060) for two time periods so there is a cancellation effect in the process. Regardless GCMs whether or not GCMs are categorized as the hot model or not, we confirmed there are no notable differences in the distributions of change factors, suggesting that the effect of hot models on climate adjustment is not significant.

Table 6 Hot models of CMIP6 GCMs used in the version 3 depending on the TCR and ECS screens. The models with 'Y' are categorized as the non-hot model group and 'N' is for the hot model group.

Modeling institution	Source Model	TCR Screen		ECS Screen	
		Likely 1.4-2.2	Very Likely 1.2-2.4	Likely 2.4-4.0	Very Likely 2.0-5.0
CAS	FGOALS-g3	Y	Y	Y	Y
INM	INM-CM4-8	N	Y	N	N
INM	INM-CM5-0	Y	Y	N	N
BCC	BCC-CSM2-MR	Y	Y	Y	Y
CMCC	CMCC-CM2-SR5	Y	Y	Y	Y
CMCC	CMCC-ESM2	Y	Y	Y	Y
CSIRO-ARCCSS	ACCESS-CM2	Y	Y	N	Y
CSIRO	ACCESS-ESM1-5	Y	Y	Y	Y
MIROC	MIROC-ES2L	N	N	Y	Y
MIROC	MIROC6	Y	Y	Y	Y
MOHC	UKESM1-0-LL	N	N	N	N
MPI-M	MPI-ESM1-2-LR	Y	Y	Y	Y
NCC	NorESM2-LM	Y	Y	Y	Y
NCC	NorESM2-MM	N	Y	N	Y
NOAA-GFDL	GFDL-ESM4	Y	Y	Y	Y
EC-Earth-Consortium	EC-Earth3	N	Y	N	Y
EC-Earth-Consortium	EC-Earth3-Veg	N	N	N	Y
EC-Earth-Consortium	EC-Earth3-Veg-LR	N	N	N	N

PDF statistics (fitted to the normal distribution), mean, and standard deviation did not show significant differences in all cases (current and future) (see Fig. 20). The results impose a high possibility that the effect of hot models might be reduced or removed in the process of estimating the fluvial change factor. Change factor is a ratio (dimensionless) between two simulated

hydrologic variables (i.e., peak flow), meaning that the hot model's effect could be canceled in the process (converting quantitative variable to dimensionless index). However, simulated time series hydrologic variables from hot models could appear to have systematic differences compared to non-hot models. The same results were confirmed in the other hot model criteria cases.

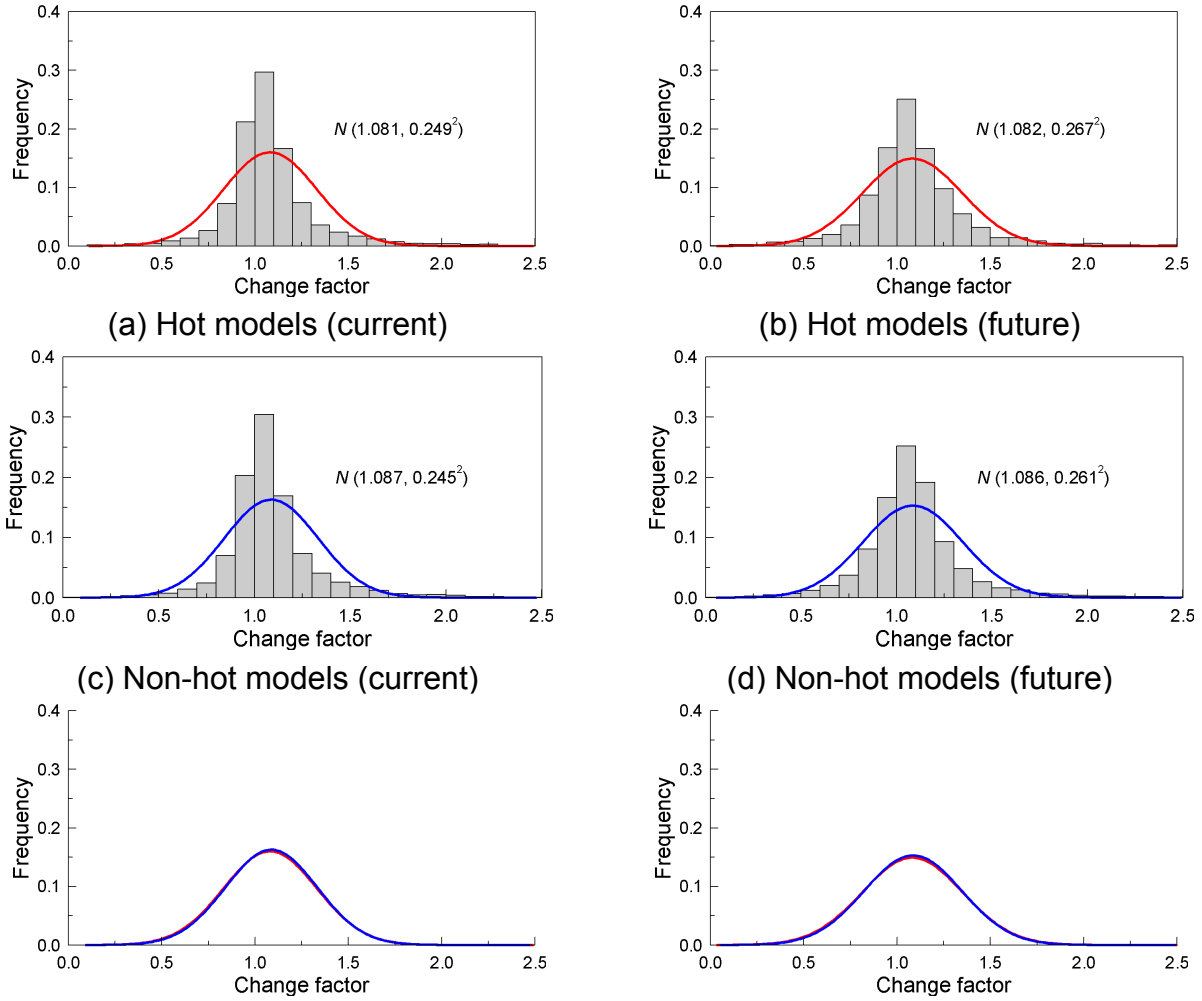

Figure 20. Comparison of change factor distributions from hot model group and non-hot model group: Left column including (a), (b), and (e) is for the current year, 2023, and right column is for the future year, 2053. In Figs (e) and (f), black, red, and blue lines indicate All models, hot models, and non-hot models, respectively. These results are for the TCR Screen (likely) 1.4-2.2, the first criterion in Table 6.

References

Adam, J.C., Clark, E.A., Lettenmaier, D.P., Wood, E.F., 2006. Correction of global precipitation products for orographic effects. Journal of Climate, 19 (1), 5-38.

Advisory Committee on Water Information (ACWI), 2018. Extreme rainfall product needs. Water information coordination program report, 1-36.

Akhtar, M., Ahmad, N., Booij, M.J., 2008. The impact of climate change on the water resources of Hindukush–Karakorum–Himalaya region under different glacier coverage scenarios. J. Hydrol. 355, 148–163.

Archuleta, C.M., Constance, E.W., Arundel, S.T., Lowe, A.J., Mantey, K.S., and Phillips, L.A., 2017, The National Map seamless digital elevation model specifications: U.S. Geological Survey Techniques and Methods, book 11, chap. B9, 39 p., https://doi.org/10.3133/tm11B9.

Barbero, R., Fowler, H.J., Lenderink, G., Blenkinsop, S., 2017. Is the intensification of precipitation extremes with global warming better detected at hourly than daily resolutions? Geophysical Research Letters, 44 (2), 974-983.

Barnes, R. (2017). Parallel non-divergent flow accumulation for trillion cell digital elevation models on desktops or clusters. Environmental modelling & software, 92, 202-212.

Beck, H. E., A. I. J. M. van Dijk, A. de Roo, D. G. Miralles, T. R. McVicar, J. Schellekens, and L.

Bergstroem, S. (1992), The HBV model—its structure and applications, SMHI Rep. RH 4, Swed. Meteorol. and Hydrol. Inst., Norrkoping, Sweden.

Bergström, S., Carlsson, B., Gardelin, M., Lindström, G., Pettersson, A., Rummukainen, M., 2001. Climate change impacts on runoff in Sweden assessments by global climate models, dynamical downscaling and hydrological modelling. Clim. Res. 16, 101–112.

Beven, K. (2006) A manifesto for the equifinality thesis. Journal of Hydrology, 320, 1-2, 18-36.

Bloschl, P. G., Sivapalan, P. M., Wagener, P. T., Viglione, D. A., and Savenije, P. H. (2013).

Booij, N., Ris, R. C., & Holthuijsen, L. H. (1999). A third-generation wave model for coastal regions 1. Model description and validation. Journal of Geophysical Research: Oceans. https://doi.org/10.1029/98JC02622

Brown, V. M., Black, A. W., Keim, B. D., 2019: Hourly rainfall climatology of Louisiana. Theor. Appl. Climatol., 137, 2011-2027.

Brown, V.M., Keim, B.D., Black, A.W., 2020. Trend analysis of multiple extreme hourly precipitation time series in the southeastern United States. Journal of Applied Meteorology and Climatology, 59 (3), 427-442.

Bruijnzeel, A. (2016), Global-scale regionalization of hydrologic model parameters, Water Resour. Res., 52, 3599–3622.

Bunya, S., Dietrich, J. C., Westerink, J. J., Ebersole, B. A., Smith, J. M., Atkinson, J. H., ... Roberts, H. J. (2010). A High-Resolution Coupled Riverine Flow, Tide, Wind, Wind Wave, and Storm Surge Model for Southern Louisiana and Mississippi. Part I: Model Development and Validation. Monthly Weather Review, 138(2), 345–377. https://doi.org/10.1175/2009MWR2906.1.

Butcher, J.B., Zi, T., Pickard, B.R., Job, S.C., Johnson, T.E. and Groza, B.A., 2021. Efficient statistical approach to develop intensity-duration-frequency curves for precipitation and runoff under future climate. Climatic change, 164 (1-2), 3.

Chavas, D.R., N. Lin, and K. Emanuel, 2015: A Model for the Complete Radial Structure of the Tropical Cyclone Wind Field. Part I: Comparison with Observed Structure. J. Atmos. Sci., 72, 3647–3662, https://doi.org/10.1175/JAS-D-15-0014.1.

Chen, D., Dai, A., 2018. Dependence of estimated precipitation frequency and intensity on data resolution. Climate dynamics, 50 (9-10), 3625-3647.

Cheng, L., AghaKouchak, A., 2014. Nonstationary precipitation intensity-duration-frequency curves for infrastructure design in a changing climate. Scientific Reports, 4 (1), 1-6.

Cho, E., Jacobs, J.M., 2020. Extreme value snow water equivalent and snowmelt for infrastructure design over the contiguous United States. Water Resources Research, 56 (10), e2020WR028126.

Cloke, H.L., Wetterhall, F., He, Y., Freer, J.E., Pappenberger, F., 2013. Modelling climate impact on floods with ensemble climate projections. Q. J. R. Meteorol. Soc. 139, 282–297.

Cohen Liechti, T., Matos, J. P., Boillat, J. L., and Schleiss, A. J. (2012). Comparison and evaluation of satellite derived precipitation products for hydrological modeling of the Zambezi River Basin. Hydrol. Earth Syst. Sci., 16, 489–500.

Dai, A., Lin, X., Hsu, K.L., 2007. The frequency, intensity, and diurnal cycle of precipitation in surface and satellite observations over low-and mid-latitudes. Climate dynamics, 29, 727-744.

Daly, C., Neilson, R.P., Phillips, D.L., 1994. A statistical-topographic model for mapping climatological precipitation over mountainous terrain. Journal of Applied Meteorology and Climatology, 33 (2), 140-158.

Daly, C., Slater, M.E., Roberti, J.A., Laseter, S.H., Swift Jr, L.W., 2017. High-resolution precipitation mapping in a mountainous watershed: ground truth for evaluating uncertainty in a national precipitation dataset. International Journal of Climatology, 37, 124-137.

Dee, D. P., et al. (2011). The ERA-Interim reanalysis: Conguration and performance of the data assimilation system. Q. J. R. Meteorol. Soc., 137, 553–597. doi:10.1002/qj.828.

Demaria, E., Dominguez, F., Hu, H., von Glinski, G., Robles, M., Skindlov, J., Walter, J., 2017b. Observed hydrologic impacts of landfalling atmospheric rivers in the Salt and Verde river basins of Arizona, United States. Water Resources Research, 53, 10025–10042.

Demaria, E., Goodrich, D., Keefer, T., 2017a. Frequency analysis of extreme sub-daily precipitation under stationary and non-stationary conditions across two contrasting hydroclimatic environments. Hydrology and Earth System Sciences Discussions, 1-28.

Dietrich, J. C., Zijlema, M., Westerink, J. J., Holthuijsen, L. H., Dawson, C., Luettich, R. A. Stone, G. W. (2011a). Modeling hurricane waves and storm surge using integrally-coupled, scalable computations. Coastal Engineering. https://doi.org/10.1016/j.coastaleng.2010.08.001.

Dietrich, J. C., Zijlema, M., Westerink, J. J., Holthuijsen, L. H., Dawson, C., Luettich, R. A., ... Stone, G. W. (2011b). Modeling hurricane waves and storm surge using integrally-coupled, scalable computations. Coastal Engineering, 58(1), 45–65. https://doi.org/10.1016/j.coastaleng.2010.08.001.

Emanuel, Kerry A. "Tropical cyclones in CMIP5 simulations." Proceedings of the National Academy of Sciences Jul 2013, 110 (30) 12219-12224; DOI: 10.1073/pnas.1301293110.

Emanuel, Kerry A. “A fast intensity simulator for tropical cyclone risk analysis.” Nat Hazards (2017) 88: 779. https://doi.org/10.1007/s11069-017-2890-7.

Fadhel, S., Rico-Ramirez, M.A., Han, D., 2017. Uncertainty of intensity–duration–frequency (IDF) curves due to varied climate baseline periods. Journal of Hydrology, 547, 600-612.

Feldmann, Monika, Kerry Emanuel, Laiyin Zhu, and Ulrike Lohmann. “Estimation of Atlantic Tropical Cyclone Rainfall Frequency in the United States.” Journal of Applied Meteorology and Climatology 58.11 (2019). DOI: https://doi.org/10.1175/JAMC-D-19-0011.1.

Feng, Z., Leung, L.R., Hagos, S., Houze, R.A., Burleyson, C.D. and Balaguru, K., 2016. More frequent intense and long-lived storms dominate the springtime trend in central US rainfall. Nature communications, 7 (1), 13429.

Ferreira, C. M., Olivera, F., & Irish, J. L. (2014). Arc StormSurge: Integrating Hurricane Storm Surge Modeling and GIS. JAWRA Journal of the American Water Resources Association, 50(1), 219–233.

Forbes, C., Luettich, R. A., Mattocks, C. A., Westerink, J. J., Forbes, C., Jr., R. A. L., ... Westerink, J. J. (2010). A Retrospective Evaluation of the Storm Surge Produced by Hurricane Gustav (2008): Forecast and Hindcast Results. Weather and Forecasting, 25(6), 1577–1602. https://doi.org/10.1175/2010WAF2222416.1.

Ganguli, P., Coulibaly, P., 2017. Does non-stationarity in rainfall require nonstationary intensity–duration–frequency curves? Hydrology and Earth System Sciences, 21 (12), 6461-6483.

Gao, Y. C., and Liu, M. F. (2013). Evaluation of high-resolution satellite precipitation products using rain gauge observations over the Tibetan Plateau. Hydrol. Earth Syst. Sci., 17, 837–849.

Garratt, J. R. (1977). Review of Drag Coefficients over Oceans and Continents. Monthly Weather Review, 105(7), 915–929.

Garzon, J., & Ferreira, C. (2016). Storm Surge Modeling in Large Estuaries: Sensitivity Analyses to Parameters and Physical Processes in the Chesapeake Bay. Journal of Marine Science and Engineering. https://doi.org/10.3390/jmse4030045.

Garzon, J., Ferreira, C., Garzon, J. L., & Ferreira, C. M. (2016). Storm Surge Modeling in Large Estuaries: Sensitivity Analyses to Parameters and Physical Processes in the Chesapeake Bay. Journal of Marine Science and Engineering, 4(3), 45. https://doi.org/10.3390/jmse4030045.

Gesch, D., Evans, G., Mauck, J., Hutchinson, J., & Carswell Jr, W. J. (2009). The national map—Elevation. US geological survey fact sheet, 3053(4).

HAD, Hydrologischer Atlas von Deutschland, 2003. Bundesministerium fuer Umwelt, Naturschutz und Reaktorsicherheit, Freiburger Verlagsdienste.

HADES, 2004. Hydrologischer Atlas der Schweiz, 2004. Bern.

Hayhoe, K., Wuebbles, D.J., Easterling, D.R., Fahey, D.W., Doherty, S., Kossin, J.P., Sweet, W.V., Vose, R.S., Wehner, M.F., 2018. Our changing climate. impacts, risks, and adaptation in the United States: The fourth national climate assessment, Volume II.

He, Y., Wetterhall, F., Cloke, H. L., Pappenberger, F., Wilson, M., Freer, J., and McGregor, G. (2009). Tracking the uncertainty in flood alerts driven by grand ensemble weather predictions. Meteorol. Appl., 16, 91–101. doi:10.1002/met.132.

Henderson, K. G., Vega, A. J., 1996: Regional precipitation variability in the southern United States. Phys. Geogr., 17, 93-112.

Herman, G.R., Schumacher, R.S., 2016. Extreme precipitation in models: An evaluation. Weather and Forecasting, 31 (6), 1853-1879.

Hettiarachchi, S., Wasko, C., Sharma, A., 2018. Increase in flood risk resulting from climate change in a developed urban watershed–the role of storm temporal patterns. Hydrology and Earth System Sciences, 22 (3), 2041-2056.

Hinzman, L.D., Kane, D.L., 1991. Snow hydrology of a headwater arctic basin: 2. Conceptual analysis and computer modeling. Water Resour. Res. 27, 1111–1121.

Hoerling, M., Eischeid, J., Perlwitz, J., Quan, X.W., Wolter, K., Cheng, L., 2016. Characterizing recent trends in US heavy precipitation. Journal of Climate, 29 (7), 2313-2332.

Hosking, J.R.M., Wallis, J.R., 2002. Regional frequency analysis: an approach based on L-moments, Cambridge Univ. Press.

Howarth, M.E., Thorncroft, C.D., Bosart, L.F., 2019. Changes in extreme precipitation in the northeast United States: 1979–2014. Journal of Hydrometeorology, 20 (4), 673-689.

Huffman, G.J., Bolvin, D.T., Nelkin, E.J., Wolff, D.B., Adler, R.F., Gu, G., Hong, Y., Bowman, K.P. and Stocker, E.F., 2007. The TRMM multisatellite precipitation analysis (TMPA): Quasi-global, multiyear, combined-sensor precipitation estimates at fine scales. Journal of hydrometeorology, 8(1), pp.38-55.

Hutchinson, M.F., Bischof, R.J. 1983. A New Method for Estimating the Spatial Distribution of Mean Seasonal and Annual Rainfall Applied to Hunter Valley, New South Wales. Australian Meteorological Magazine. 31, 179-184.

Hydrologischer Atlas Österreichs (HAÖ), 2003. Bundesministerium für Landund Forstwirtschaft, Umwelt und Wasserwirtschaft, Österreichischer Kunst- und Kulturverlag, Wien.

Janssen, E., Wuebbles, D.J., Kunkel, K.E., Olsen, S.C., Goodman, A., 2014. Observational- and model-based trends and projections of extreme precipitation over the contiguous United States. Earth's Future, 2, 99-113.

Joyce, R. J., Janowiak, J. E., Arkin, P. A., and Xie, P. (2004), CMORPH: A method that produces global precipitation estimates from passive microwave and infrared data at high spatial and temporal resolution. J. Hydrometeorol., 5, 487–503.

K. P., and Stocker, E. F. (2007). The TRMM Multisatellite Precipitation Analysis (TMPA): Quasi-global, multiyear, combined-sensor precipitation estimates at ne scales. J. Hydrometeorol., 8, 38–55. doi:10.1175/JHM560.1.

Kalnay E, Kanamitsu M, Kistler R, Collins W, Deaven D, Gandin L, Iredell M, Saha S, White G, Woollen J, Zhu Y, Leetmaa A, Reynolds R, Chelliah M, Ebisuzaki W, Higgins W, Janowiak J, Mo KC, Ropelewski C, Wang J, Jenne R, Joseph D (1996) The NCEP/NCAR 40-year reanalysis project. Bull Am Meteorol Soc 77(3):437–471.

Kao, S-C., DeNeale, S.T., Yegorova, E., Kanney, J., Carr, M.L., 2020. Variability of precipitation areal reduction factors in the conterminous United States. Journal of Hydrology X, 9, 100064.

Karl TR, Knight RW. 1998. Secular trends of precipitation amount, frequency, and intensity in the United States. Bulletin of the American Meteorological Society, 79, 231–241.

Keef, C., Svensson, C., & Tawn, J. A. (2009). Spatial dependence in extreme river ows and precipitation for Great Britain. Journal of Hydrology, 378(3-4), 240–252. https://doi.org/10.1016/j.jhydrol.2009.09.026.

Keefer, T.O., Renard, K.G., Goodrich, D.C., Heilman, P., Unkrich, C., 2016. Quantifying extreme rainfall events and their hydrologic response in southeastern Arizona. Journal of Hydrologic Engineering, 21(1), 04015054.

Kerr, P. C., Martyr, R. C., Donahue, A. S., Hope, M. E., Westerink, J. J., Luettich, R. A., ... Westerink, H. J. (2013). U.S. IOOS coastal and ocean modeling testbed: Evaluation of tide, wave, and hurricane surge response sensitivities to mesh resolution and friction in the Gulf of Mexico: IOOS TESTBED-RESOLUTION AND FRICTION. Journal of Geophysical Research: Oceans, 118(9), 4633–4661. https://doi.org/10.1002/jgrc.20305

Kharin, V.V., Zwiers, F.W. 2000. Changes in the extreme in an ensemble of transient climate simulations with a coupled atmosphere-ocean GCM. Journal of Climate, 13, 3760-3788.

Kidd, C., Bauer, P., Turk, J., Huffman, G. J., Joyce, R., Hsu, K. L., and Braithwaite, D. (2012). Intercomparison of high-resolution precipitation products over Northwest Europe. J. Hydrometeorol., 13, 67–83. doi:10.1175/JHM-D-11-042.1.

Kim, J., Johnson, L., Cifelli, R., Thorstensen, A., Chandrasekar, V., 2019. Assessment of antecedent moisture condition on flood frequency: An experimental study in Napa River Basin, CA. Journal of Hydrology: Regional Studies, 26, 100629.

Kim, J., Shu, E., Lai, K., Amodeo, M., Porter, J., Kearns, E., 2022. Assessment of the standard precipitation frequency estimates in the United States. Journal of Hydrology: Regional Studies, 44, 101276.

Knapp, K. R., H. J. Diamond, J. P. Kossin, M. C. Kruk, C. J. Schreck, 2018: International Best Track Archive for Climate Stewardship (IBTrACS) Project, Version 4. Version 4 revision 00. NOAA National Centers for Environmental Information. non-government domain https://doi.org/10.25921/82ty-9e16. Retrieved October 20, 2019.

Knapp, K. R., M. C. Kruk, D. H. Levinson, H. J. Diamond, and C. J. Neumann, 2010: The International Best Track Archive for Climate Stewardship (IBTrACS): Unifying tropical cyclone best track data. Bulletin of the American Meteorological Society, 91, 363-376.

Konrad, C.P., Dettinger, M.D., 2017. Flood runoff in relation to water vapor transport by atmospheric rivers over the western United States, 1949–2015. Geophysical Research Letters, 44 (22), 11-456.

Kopp, Robert E., Radley M. Horton, Christopher M. Little, Jerry X. Mitrovica, Michael Oppenheimer, D. J. Rasmussen, Benjamin H. Strauss, Claudia Tebaldi. Probabilistic 21st and 22nd century sea-level projections at a global network of tide-gauge sites. Earth's Future 2.8 (2014): 383-406. DOI: 10.1002/2014EF000239.

Kunkel, K.E., Andsager, K., Easterling, D.R., 1999. Long-term trends in extreme precipitation events over the conterminous United States and Canada. Journal of Climate, 12 (8), 2515-2527.

Lehner, B., and Grill, G. (2013). Global river hydrography and network routing: Baseline data and new approaches to study the world's large river systems. Hydrological Processes, 27(15), 2171–2186. https://doi.org/10.1002/hyp.9740.

Li, Z., Tang, G., Kirstetter, P., Gao, S., Li, J.L., Wen, Y., Hong, Y., 2022. Evaluation of GPM IMERG and its constellations in extreme events over the conterminous united states. Journal of Hydrology, 606, 127357.

Lopez-Cantu, T., Samaras, C., 2018. Temporal and spatial evaluation of stormwater engineering standards reveals risks and priorities across the United States. Environmental Research Letters, 13 (7), 074006.

Lopez-Cantu, T., Prein, A.F., Samaras, C., 2020. Uncertainties in future US extreme precipitation from downscaled climate projections. Geophysical Research Letters, 47 (9), e2019GL086797.

Loukas, A., Vasiliades, L., Dalezios, N.R., Domenikiotis, C., 2001. Rainfall-frequency mapping for Greece. Physics and chemistry of the earth, Part B: hydrology, oceans and atmosphere, 26 (9), 669-674.

Lu, P., N. Lin, K. Emanuel, D. Chavas, and J. Smith, 2018: Assessing hurricane rainfall mechanisms using a physics-based model: Hurricanes Isabel (2003) and Irene (2011). J. Atmos. Sci., 75, 2337-2358, doi:10.1175/jas-d-17-0264.1.

Luettich, R. A., Westerink, J. J., & Scheffner, N. (1992). ADCIRC: an advanced three-dimensional circulation model for shelves coasts and estuaries, report 1: theory and methodology of ADCIRC-2DDI and ADCIRC-3DL. Dredging Research Program Technical Report DRP-92-6, U.S. Army Engineers Waterways Experiment Station, Vicksburg, MS.

Mandli, Kyle T., and Clint N. Dawson. “Adaptive Mesh Refinement for Storm Surge.” Ocean Modelling 75 (2014): 36–50. DOI: 10.1016/j.ocemod.2014.01.002.

Markus, M., Angel, J., Byard, G., McConkey, S., Zhang, C., Cai, X., Notaro, M., Ashfaq, M., 2018. Communicating the impacts of projected climate change on heavy rainfall using a weighted ensemble approach. Journal of Hydrologic Engineering, 23 (4), 04018004.

Marsooli, R., Lin, N., Emanuel, K. et al. “Climate change exacerbates hurricane flood hazards along US Atlantic and Gulf Coasts in spatially varying patterns.” Nat Commun 10, 3785 (2019) doi:10.1038/s41467-019-11755-z.

McEnroe, B.M., Young, C.B., 2014. Development of new precipitation frequency tables for counties in Kansas using NOAA Atlas 14 (No. KS-14-13). Kansas. Dept. of Transportation. Bureau of Materials & Research.

McGraw, D., Nikolopoulos, E.I., Marra, F., Anagnostou, E.N., 2019. Precipitation frequency analyses based on radar estimates: An evaluation over the contiguous United States. Journal of Hydrology, 573, 299-310.

Meinshausen, M.; et al. (November 2011), "The RCP greenhouse gas concentrations and their extensions from 1765 to 2300", Climatic Change, 109 (1–2): 213–241, doi:10.1007/s10584-011- 0156-z.

Miller, R.J., A.J. Schrader, C.R. Sampson, and T.L. Tsui, 1990: The Automated Tropical Cyclone Forecasting System (ATCF). Wea. Forecasting, 5, 653–660, https://doi.org/10.1175/1520-0434(1990)005<0653:TATCFS>2.0.CO;2.

Myhre, G., Alterskjær, K., Stjern, C.W., Hodnebrog, Ø., Marelle, L., Samset, B.H., Sillmann, J., Schaller, N., Fischer, E., Schulz, M., Stohl, A., 2019. Frequency of extreme precipitation

increases extensively with event rareness under global warming. Scientific reports, 9 (1), 16063.

Neal, J.C., Dunne, T., Sampson. C.C., Smith, A., & Bates, P., (2018). Optimisation of the two-dimensional hydraulic model LISFOOD-FP for CPU architecture, Environmental Modelling and Software, 107, 148-157, doi: 10.1016/j.envsoft.2018.05.011.

Neal, J.C., Fewtrell, T.J., and Trigg, M. (2009), Parallelisation of storage cell flood models using OpenMP, Environ. Modell. Software, 24, 872–877, doi:10.1016/j.envsoft.2008.12.004.

Neal, J.C., Fewtrell, T.J., Bates, P.D., and Wright, N.G., (2010), A comparison of three parallelisation methods for 2D flood inundation models, Environ. Modell. Software, 25, 398–411, doi:10.1016/j.envsoft.2009.11.007.

Neal, J.C., Schumann, G., and Bates, P.D., (2012), A subgrid channel model for simulating river hydraulics and floodplain inundation over large and data sparse areas, Water Resour. Res., 48, W11506, doi:10.1029/2012WR012514.

O'Callaghan, J. F., & Mark, D. M. (1984). The extraction of drainage networks from digital elevation data. Computer vision, graphics, and image processing, 28(3), 323-344.

Partridge, T.F., Winter, J.M., Osterberg, E.C., Hyndman, D.W., Kendall, A.D., Magilligan, F. J., 2018. Spatially distinct seasonal patterns and forcings of the U.S. warming hole. Geophys. Res. Lett., 45, 2055–2063.

Pendergrass, A.G., Knutti, R., Lehner, F., Deser, C., Sanderson, B.M., 2017. Precipitation variability increases in a warmer climate. Scientific reports, 7 (1), 17966.

Perica, S., Pavlovic, S., St Laurent, M., Trypaluk, C., Unruh, D., Wilhite, O., 2018. Precipitation-Frequency Atlas of the United States. Volume 11, Version 2.0. Texas.

Prein, A.F., Mearns, L.O., 2021. US extreme precipitation weather types increased in frequency during the 20th century. Journal of Geophysical Research: Atmospheres, 126 (7), e2020JD034287.

Prein, A.F., Rasmussen, R.M., Ikeda, K., Liu, C., Clark, M.P., Holland, G.J., 2017. The future intensification of hourly precipitation extremes. Nature climate change, 7 (1), 48-52.

Pytides, version 0.0.6. Maritime Planning Associates, 2018. GitHub, https://github.com/maritimeplanning/pytides.

Quinn, N., Bates, P.D., Neal, J., Smith, A., Wing, O., Sampson, C., Smith, J., and Heffernan, J. (2019). The spatial dependence of flood hazard and risk in the United States. Water Resources Research, 55, 1890-1911. http://doi.org/10.1029/2018WR024205.

Ragno, E., AghaKouchak, A., Love, C.A., Cheng, L., Vahedifard, F., Lima, C.H.R., 2018. Quantifying changes in future intensity-duration-frequency curves using multimodel ensemble simulations. Water Resources Research, 54, 1751-1764.

Rahmani, V., Harrington Jr, J., 2019. Assessment of climate change for extreme precipitation indices: A case study from the central United States. International Journal of Climatology, 39 (2), 1013-1025.

Ropelewski, C. F., M. S. Halpert, 1986. North American precipitation and temperature patterns associated with the El Niño/Southern Oscillation (ENSO). Mon. Wea. Rev., 114, 2352-2362.

Running, S.W., Nemani, R.R., Hungerford, R.D., 1987. Extrapolation of synoptic meteorological data in mountainous terrain and its use for simulating forest evapotranspiration and photosynthesis. Canadian Journal of Forest Research, 17 (6), 472-483.

Runoff Prediction in Ungauged Basins: Synthesis across Processes, Places and Scales, Cambridge Univ. Press, Cambridge, U. K.

Salathé Jr., E.P., 2006. Influences of a shift in North Pacific storm tracks on western North American precipitation under global warming. Geophysical Research Letters, 33 (19).

Sampson, C. C., Bates, P.D., Neal, J.C., & Horritt, M.S. (2013), An automated routing methodology to enable direct rainfall in high resolution shallow water models, Hydrol. Processes, 27, 467–476, doi:10.1002/hyp.9515.

Sampson, C. C., Fewtrell, T. J., O'Loughlin, F., Pappenberger, F., Bates, P. B., Freer, J. E., and Cloke, H. L. (2014), The impact of uncertain precipitation data on insurance loss estimates using a Flood Catastrophe Model. Hydrol. Earth Syst. Sci. Discuss., 11, 31–81. doi:10.5194/hessd-11-31-2014.

Sampson, C. C., Smith, A. M., Bates, P. D., Neal, J. C., Alleri, L., and Freer, J. E. (2015). A high-resolution global food hazard model. Water Resources Research, 51, 7358–7381. https://doi.org/10.1002/2015WR016954.

Seibert, J., 1997. Estimation of Parameter Uncertainty in the HBV ModelPaper presented at the Nordic Hydrological Conference (Akureyri, Iceland-August 1996). Hydrol. Res. 28, 247–262.

Seibert, J., and M. J. P. Vis (2012), Teaching hydrological modeling with a user-friendly catchment-runoff-model software package, Hydrol. Earth Syst. Sci., 16(9), 3315–3325.

Shrestha, A., Garcia, M., 2023. Influence of Precipitation Uncertainty and Land Use Change on the Optimal Catchment Scale Configuration of Green Stormwater Infrastructure. Journal of Sustainable Water in the Built Environment, 9 (2), 04023001.

Silva, D.F., Simonovic, S.P., Schardong, A., Goldenfum, J.A., 2021. Assessment of non-stationary IDF curves under a changing climate: Case study of different climatic zones in Canada. Journal of Hydrology: Regional Studies, 36, 100870.

Simley, J. D., & Carswell Jr, W. J. (2009). The national map—hydrography. US Geological Survey Fact Sheet, 3054(4).

Smith, A., Freer, J., Bates, P., Sampson, C., 2014. Comparing ensemble projections of flooding against flood estimation by continuous simulation. J. Hydrol. 511, 205–219.

Smith, A., Sampson, C., and Bates, P. (2015), Regional food frequency analysis at the global scale. Water Resour. Res., 51, 539–553. doi: 10.1002/2014WR015814.

Stillman, S.T., 1996. A comparison of three automated precipitation simulation models: ANUSPLIN, MTCLIM-3D, and PRISM (Doctoral dissertation, Montana State University-Bozeman, College of Letters & Science).

Sun, N., Yan, H., Wigmosta, M.S., Coleman, A.M., Leung, L.R., Hou, Z., 2022. Datasets for characterizing extreme events relevant to hydrologic design over the conterminous United States. Scientific Data, 9 (1), 154.

Tabari, H., 2020. Climate change impact on flood and extreme precipitation increases with water availability. Scientific Reports, 10 (1), 1-10.

Teutschbein, C., Wetterhall, F., Seibert, J., 2011. Evaluation of different downscaling techniques for hydrological climate-change impact studies at the catchment scale. Clim. Dyn. 37, 2087–2105.

Thompson, C.S., 2002, March. The high intensity rainfall design system: HIRDS. In International Conference on Flood Estimation, Bern, Switzerland, 6-8.

Tozer, B, Sandwell, D. T., Smith, W. H. F., Olson, C., Beale, J. R., & Wessel, P. (2019). Global bathymetry and topography at 15 arcsec: SRTM15+. Earth and Space Science. 6. https://doi.org/10.1029/ 2019EA000658

Um, M.J., Heo, J.H., Markus, M., Wuebbles, D.J., 2018. Performance evaluation of four statistical tests for trend and non-stationarity and assessment of observed and projected annual maximum precipitation series in Major United States cities. Water Resources Management, 32, 913-933.

USGS. (2019). Guidelines for Determining Flood Flow Frequency: Bulletin 17. Chapter 5 of Section B, Surface Water: Book 4, Hydrologic Analysis and Interpretation.

Viale, M., Garreaud, R., 2015. Orographic effects of the subtropical and extratropical Andes on upwind precipitating clouds. Journal of Geophysical Research: Atmospheres, 120 (10), 4962-4974.

Vitousek, S, Barndard, PL & P Limber. (2017). Can Beaches Survive Climate Change? Earth and Space Science. Apr. 2017.

Wahba, G., 1980. Spline bases, regularization, and generalized cross validation for solving approximation problems with large quantities of noisy data. University of WISCONSIN.

Wahl, T., Jain, S., Bender, J., Meyers, S.D., Luther, M.E. (2015). Increasing risk of compound flooding from storm surge and rainfall for major US cities. Nature Climate Change, 5, 1093-1097, doi:10.1038/nclimate2736.

Walega, A., Amatya, D.M., Caldwell, P., Marion, D., Panda, S., 2020. Assessment of storm direct runoff and peak flow rates using improved SCS-CN models for selected forested watersheds in the Southeastern United States. Journal of Hydrology: Regional Studies, 27, 100645.

Ward, J. P., Couasnon, A., Eilander, D., Haigh, I.D., Hendry, A., Muis, S., Veldkamp, T.I.E., Winsemius, H.C., Wahl, T. (2018). Dependence between high sea-level and high river discharge increases flood hazard in global deltas and estuaries. Environmental Research Letters, 13, 084012, doi: https://doi.org/10.1088/1748-9326/aad400.

Wuebbles, D., Meehl, G., Hayhoe, K., Karl, T.R., Kunkel, K., Santer, B., Wehner, M., Colle, B., Fischer, E.M., Fu, R., Goodman, A., 2014. CMIP5 climate model analyses: climate extremes in the United States. Bulletin of the American Meteorological Society, 95 (4), 571-583.

Xie, P., Chen, M., Yang, S., Yatagai, A., Hayasaka, T., Fukushima, Y., and Liu, C. (2007), A gauge-based analysis of daily precipitation over East Asia. J. Hydrometeorolgy., 8, 607–626. doi:10.1175/JHM583.1.

Yan, H., Sun, N., Chen, X., Wigmosta, M.S., 2020. Next-generation intensity-duration-frequency curves for climate-resilient infrastructure design: Advances and opportunities. Frontiers in Water, 2, 545051.

Yan, H., Sun, N., Wigmosta, M., Skaggs, R., Hou, Z., Leung, R., 2018. Next-generation intensity-duration-frequency curves for hydrologic design in snow-dominated environments. Water Resources Research, 54 (2), 1093-1108.

Zhu, J. 2012a. Impact of climate change on extreme rainfall across the United States. ASCE Journal of Hydrologic Engineering, 18 (10).

Zhu, J., Forsee, W., Schumer, R., Gautam, M., 2013. Future projections and uncertainty assessment of extreme rainfall intensity in the United States from an ensemble of climate models. Climate Change, 118, 469-485.

Zhu, J., Stone, M. C., Forsee, W. 2012b. Analysis of potential impacts of climate change on intensity-duration-frequency (IDF) relationships for six regions in the United States. Journal of Water and Climate Change, 3 (3), 185-196.

Appendix

A. Historical Analysis

Overview

The historical portion of the analysis concerns the recreation of past flooding events in two different contexts, inland and coastal. The inland methodology begins with observed precipitation and stream gauge discharge, which are used to recreate flooding extents with combined pluvial and fluvial simulations. The coastal methodology centers on recreating historical extreme surge events with a combination of hydrodynamic modeling, remote sensing, interpolations, and statistical modeling.

Event-based flood modeling: Coastal

The historical storm recreation on the coast relies heavily on the ADCIRC model runs that have been created to simulate water levels associated with each of the modeled storms. The numerical simulations of storm surges are based on the coupled version (Dietrich et al., 2011a) of the ADCIRC hydrodynamic model (Luettich, Westerink, & Scheffner, 1992) and the wave model SWAN (Booij, Ris, & Holthuijsen, 1999) to simulate waves and hydrodynamics from tides, hurricanes, and Nor'easters. ADCIRC is a finite element, shallow water model that solves for water levels and currents at a range of scales and is widely used for storm surge modeling (Bunya et al., 2010; Forbes et al., 2010; Garzon & Ferreira, 2016). SWAN is a third-generation spectral wave model that computes random, short-crested wind-generated waves and wave transformation in near-shore and inland waters for the purpose of including mean wave effects on surge elevations (Garzon & Ferreira, 2016). Simulations were performed in the context of a supercomputing environment provided by the Extreme Science and Engineering Discovery Environment (XSEDE), supported by the National Science Foundation (NSF).

The performance of ADCIRC+SWAN to simulate hurricane storm surge was validated through the U.S. IOOS modeling test bed (Kerr et al., 2013), and the performance and scalability of the coupled ADCIRC+SWAN model were tested successfully with up to 9,216 cores (Dietrich et al., 2011b) in a High-Performance Computing (HPC) environment. Tidal forcing from seven tidal constituents was incorporated based on the Western North Atlantic, Caribbean, and Gulf of Mexico Tidal Databases. The land cover and land use information are represented in the model by parameterizing the shear

stress on the sea bottom as well as on the free sea surface. Manning's roughness coefficient is applied to address different sea bed surfaces and respective frictional resistance by different land cover in the study areas. Additionally, using Garratt's drag law (Garratt, 1977), the model accounts for a reduction in wind shear stress on the sea surface due to canopies and other land uses present in the model domain. Friction parameters in the model are computed using the land cover information collected from several national land cover databases such as the National Land Cover Dataset (NLCD). For example, the Mason Flood Hazards Research Lab has developed several numerical meshes specially designed for the Mid-Atlantic Region and the Chesapeake Bay (resolution of approximately 30 meters in the Chesapeake Bay region). NOAA has recently developed the HSOFS covering the entire U.S. East Coast and Gulf of Mexico (GOM) with ~1.8 million nodes and an approximate resolution of 160^{+} meters. The simulations are based primarily on existing numerical meshes for the region of interest based on each individual landfall location.

For this study, variations of the best available meshes for each study area were applied according to the hurricane tracks and the impacted areas. Historical storms were simulated based on an asymmetric wind model forced by the National Hurricane Center (NHC) best track databases, the North American Mesoscale Forecast System (NAM) developed by the National Centers for Environmental Prediction (NCEP), and any additional publicly available weather dataset to ensure the best representation of the wind and pressure fields for each of the historic storms. The results demonstrated that while the NAM presented the best results in hindcasting selected historical storm surges in the Chesapeake Bay, other systems might better represent the atmospheric fields for different storms and locations (Garzon et al. 2018). Historical hindcasting and validation of the modeling framework were performed based on high water marks, USGS and NOAA tide gages, and any other available data. A model validation report will be produced to document the model performance for each storm and location. Coastal flooding inundation maps will be produced based on a GIS framework based on ArcStormSurge (Ferreira, Olivera, & Irish, 2014) that will be used to convert the model outputs, creating spatial and temporal tropical storms inundation maps, wave heights, and maximum inundation extent. The downscaling of the coupled ADCIRC+SWAN-produced results will be performed using the GRASS-based Kalpana script. This script uses the extrapolation module "grow" to extend the water levels to the same elevation on the high-resolution DEM. These maps will incorporate the resulting water levels from storm surges, tides, and waves, streamlining the flood map delineation. Each historical storm simulation is documented in Jupyter notebooks demonstrating the model validation and specific methods utilized

for the study. The final layer presents inundation with water depths, as shown in Fig. 21.

Figure 21: Flood hazard layer for Hurricane Harvey (September 2017): 24,466 buildings impacted in Galveston County

Event-based flood modeling: Inland

Historical inland flood event footprints will be simulated using the FSF-FM modeling framework. This will be undertaken by linking the modeling framework to the USGS gauge network to simulate observed events explicitly. These hindcast simulations will be limited to simulations of large-magnitude events on relatively large fluvial floodplains. An upstream area threshold of 10,000km^2 was applied with a minimum annual exceedance probability of 0.98. A minimum observational gauge record length of 50 years was also applied. An examination of the USGS observational record yielded ~150 observed events suitable for hindcast simulation. Each event simulation was undertaken using the observed event hydrograph from the gauge record, implementing the hydrograph as a boundary condition in the FSF-FM modeling framework. Given the known uncertainties in measuring discharge during extreme events, each observed event will be simulated within an uncertainty framework, exploring uncertainty around observed peak flows. A Monte Carlo sampling approach will be used to sample from an assumed normal distribution of errors around the observed peak hydrograph, with errors ranging from +20% to minus 20%. Each sample of this error space will yield a separate simulation, providing numerous realizations of the event footprint.

B. Localization

B-1. Adaptations

Overview

To supplement the model data on hydraulic characteristics, it is also important to capture information on hydro-modifications made through human intervention. In many places, urbanization and development has caused changes to natural flows, and infrastructure protects communities in ways that may not always be captured in the inputs to the flood models. Flood adaptation infrastructure are built works projects constructed in flood prone areas to mitigate the risk of flooding. The purpose of adding flood adaptation structures to our modeling process is to increase the accuracy of our flood inundation layers. Flood adaptation projects can generally be categorized as (1) traditional hard engineering or “grey” infrastructure, such as levees, dams, hardened ditches, etc., or (2) nature-based soft or “green” infrastructure projects designed to mimic nature, capturing and slowing the advance of floodwaters (e.g. wetland creation, living shorelines, mangrove planting, etc.). Policy-driven, non-structural flood adaptation also exists, however, the following discussion pertains to physical grey and green infrastructure adaptation. Only adaptation measures that are currently built and operational were included in the data. The goal of the exercise is to show how today environment is interacting with flooding, and projecting future projects was deemed too uncertain to include.

There are five modeling mechanisms through which the flood reduction potential of adaptation infrastructure projects are incorporated into the modeled flood inundation layers:

1. Return period — Modeled flooding is excluded within the adaptation structure’s service area for all modeled flood events up to the return period year for which the structure is rated (e.g. 10-year).
2. Reduction percentage — Modeled flooding is reduced by an assumed percentage within the estimated service area behind an adaptation structure designed to mitigate flooding.
3. Increased infiltration rate — Soil infiltration rates associated with the soils data underpinning FSF internal hydraulic models are modified within the footprints of adaptation projects to

increase infiltration within these areas. This mimics the flood reduction impact of these structures.

4. Friction parameter — Modeled flooding in coastal areas is reduced by an assumed percentage within the estimated service area behind adaptation structures such as coral reefs and oyster beds. The momentum of advancing floodwaters is dissipated by friction related to the roughness of the substrate over which the water is moving and the resulting "choppiness" of turbulent surface water. This friction is increased by structures like coral reefs and oyster beds.
5. Elevation model edit — When the elevation of a structure such as a levee or a seawall is known, but its return period is not, the structure's average elevation is added to the entire service area to better reflect the protection that the structure provides.

Adaptation data collection efforts were divided into two separate work streams: coastal adaptation and inland adaptation. This was related to the dominant influence of tidal flooding and storm surge in coastal regions, whereas these variables don't impact flooding in inland regions. Because of differing flood drivers in coastal and inland regions, adaptation infrastructure projects tend to vary regionally as well. Focusing research efforts through the lens of coastal versus inland flooding allowed the adaptation team to be more focused and efficient throughout our data collection efforts.

Grey Adaptation: Levees, Dams, and Others

Levees are the most ubiquitous and widely applied adaptation structure incorporated into the FSF-FM flood inundation layers. Levees are an example of "grey" infrastructure and are defined by the US Army Corps of Engineers (USACE) as man-made barriers along a water course, constructed for the primary purpose of providing flood, storm, and hurricane protection. Levees are used to mitigate flooding in both coastal and inland areas. Levees were incorporated into FSF-FM flood inundation layers using the "return period" mechanism described above. The adaptation return period mechanism is applied during a part of the modeling process where it does have an impact on areas downstream of the adaptation area. Water is not removed from these adaptation zones as a post-processing step but rather through its incorporation as a modeling input. The water is "forced" to travel somewhere else since it cannot enter the adaptation zones as defined by the return periods assigned to the applicable adaptation features.

Multiple data sources were used to identify levees to be incorporated into the model. The USACE National Levee Database (NLD) is the most comprehensive inventory of levees within the U.S., containing data on roughly 30% of the country's existing levees (Wing 2017). Nearly all levee data incorporated into the flood models came from NLD. This includes spatial data representing the service areas protected by levees, and the level of protection offered by these levees (e.g. return period maximum for which the levee protects). Additional levee projects were visually identified with the support of a DEM-driven elevation ridge modeling approach. Additional data on levees was derived from news articles, USACE technical manuals, visual inspection of internally modeled flood data, and assumptions based on level of protection offered by levees for which documentation was limited.

Dams are another nationally ubiquitous type of grey adaptation. They are structures that are designed to impound and utilize the flow of water for multiple purposes, including flood control. Dams are used to mitigate flooding in both coastal and inland areas. Dams were incorporated into FSF modeled flood inundation layers using the "return period" mechanism described above. The National Inventory of Dams (NID) provided the spatial and hazard classification data for dams. Dams in the NID database were assigned return periods associated with the spillway design capacity. When unavailable, the 2012 FEMA Summary of Existing Guidelines for Hydrologic Safety of Dams was utilized to assign return periods. The flood protection service areas of dams were based on availability of inundation maps according to the dam's Emergency Action Plan. Service areas were captured by downloading available shapefiles or by digitizing them manually. When the spatial extents of a dam's service area of flood protection couldn't be found in documentation, service areas were digitized manually. This was done at the location of the adaptation structure by overlaying the internally modeled flooding extents of the return period year that matches the return period for which the structure was designed. This procedure was used to estimate where flooding should logically be removed.

Flooding caused by high tides and storm surge along tidal rivers can also be prevented by dams. Major dams in coastal regions block the influx of tidal floodwaters upstream of the dam's location on the river. NID was used to identify dams in coastal areas, and service areas upstream of the dam were manually digitized to represent the area where tidal waters cannot feasibly reach, based on elevation of the dam. The area was assumed to reduce flooding by 100% and a maximum return period of protection was assigned, if known.

Additional research was conducted to ensure that a comprehensive inventory of adaptation projects beyond levees and dams was incorporated into the modeled flood layers. FEMA Flood Insurance Studies (FIS) provide a detailed narrative of “principal flood problems” and “flood protection measures” that have been documented at the county level throughout the U.S. These FIS reports were used to investigate the presence of any additional flood protection present beyond the levees and dams accounted for in the NLD and NID within a county. The reports also revealed the existence of levees and dams not accounted for within the NLD and NID.

Grey infrastructure projects outside of levees and dams were often identified using FIS reports and incorporated into the modeled flood layers by generally applying the “return period” method. FIS reports would often provide a return period for which the structure was designed to protect. When a return period wasn’t provided in the FIS, further research was conducted in order to assign a return period. FIS generally did not provide the spatial data representing the service areas for which a project protects. Service areas were therefore digitized manually at the location of the adaptation structure by overlaying the internally modeled flooding extents of the return period year that matches the return period for which the structure was designed. This procedure was used to estimate where flooding should logically be removed. Following inspection of FIS reports, a general web search of the county was completed to find any additional information on adaptation.

Green Adaptation: Green Infrastructure and Soils

Green infrastructure adaptation projects are designed to mimic natural systems to reduce flooding. These green adaptation projects rely on natural materials like plants and soils to capture, slow, and infiltrate the advance of floodwaters. This differs from most grey infrastructure projects that reduce flooding by physically excluding water from a service area (e.g. levees, dams, seawalls, etc.), or by rapidly moving flood water out of the structure’s service area (e.g. hardened ditches, emergency spillways, etc.). The flood reduction impacts of green infrastructure were, therefore, generally incorporated into the modeled flood inundation layers through the use of the “reduction percentage” and “increased infiltration rate” methodologies described above. While these features are not part of our main target for this version of the adaptation dataset, when we do find features like stormwater basins, catch basins, retention ponds, rain gardens, etc. we include them in our increased infiltration rate methodology. A newer methodology that we have incorporated into our

adaptation workstream is called “conveyance” and it will be described in greater detail in the second release of the technical document. In short, the conveyance method incorporates channels into our model that we know have been enhanced, fortified or deepened such that we can apply a return period for inclusion in the water source aspect of our flood modeling process. In the future, we would like to figure out ways in which we can find, digitize and include in future iterations.

The use of soils data was critical to both the overall hydrologic model and the modeling mechanism used to incorporate green infrastructure into FSF-FM flood layers. Internal fluvial and pluvial hydraulic flood models relied on the national USDA Gridded Soil Survey Geographic Database (gSSURGO) to provide the soil infiltration rates required to model overland flows and resultant flooding during flood events. The gSSURGO dataset was used for its superior spatial resolution compared to other national soil database alternatives (e.g. UN Harmonized World Soil Database). Soil infiltration rates were based on hydrologic soil groups assigned to the mapped soil types within gSSURGO. Hydrologic soil groups ranged from Group A (highest infiltration rate; well drained to excessively drained sands or gravelly sands) to Group D (lowest infiltration rate; consists chiefly of clays). Soils were integral in incorporating green infrastructure projects into the modeled flood inundation layers using the “increased infiltration rate” mechanism described above.

Coastal Adaptation

Accounting for the diversified approach to coastal flood risk prevention, from structural flood protection measures to natural solutions, better reflects real-world scenarios. Incorporating these adaptation measures into the research stream greatly increases the accuracy of the flood hazard layers. Researching and locating green and grey infrastructure allows areas to be marked as either protected or semi-protected from flooding. Close attention is paid to whether a structure is designed to protect against tidal flooding, storm surge, or both. Additionally, in the case of seawalls, the relative heights (elevation above nearby ground surface) are collected in order to model overtopping scenarios. Digital elevation models are altered to reflect these relative heights.

For tracking dams, seawalls, shoreline characteristics, and natural areas, researchers relied on resources such as the State-level GIS databases, Coastal Zone Management Authorities, the Georgetown Climate Adaptation Clearinghouse, and groups such as the American Society of Adaptation Professionals (ASAP). This research is redone at the local level once initial (lower

resolution) inundation layers have been produced and analyzed for areas with more than 50 homes inundated. Levees, hurricane barriers, and dams are incorporated from the NLD or the NID, both provided by USACE.

The first round of inundation modeling is exported at a low-resolution raster file. This file is used to determine “hot spots” of flooding by visualizing greatly impacted places. These locations identified through this visualization process are the focus of the next round of research on tidal flooding reports.

News reports, public meeting minutes, foundation-funded studies, university papers, and environmental, and planning nonprofit reports all provide insights on local histories of flooding and the construction of flood-protection infrastructure. Within these reports, it is able to find information on when certain types of infrastructure were built, how much it cost, who paid for it, the community or area it serves (protects), and what type of scenario it was created for. Within this research stream, a great deal is learned about what type of flooding is most intrusive to a place and what has been done to address it. From there, local or state officials are contacted to see if the adaptation structure has been digitized and if not, then it is included for later digitizing into the final adaptation service area file.

Once as much data as possible is gathered on adaptation structures and the areas they protect from flooding events, these data are digitized into polygon service areas. Some adaptation infrastructure completely protect an area (e.g. levees), while other methods reduce water depth (e.g. pumps). Areas that get completely removed from the flood layers are mostly leveed areas or those behind hurricane protection systems. Attention is paid to what scenario the systems were built to withstand. For example, if a barrier can only sustain floods related to the worst-case scenario for a category 2 storm, then flooding will not be removed from hurricane category 3^{+} scenarios. Note since we cannot know how the structure will prevent any given amount of flooding in the event of a failure, we assume a total failure at the point past the structure’s design in the modeling process. Having adaptation areas represented in the DEM allows for the model to capture the “x amount of flooding at the point of failure” value automatically when we move to a return period beyond the one indicated for the adaptation feature. For features not represented in the DEM, either because they are very narrow, small, or built underground, a total failure is assumed.

The structure of the adaptation service area files includes the name of the structure, the type of structure, the event the structure protects the area from (tidal, hurricane, pluvial, or fluvial), the return period, the soil change category, the reduction percentage, state, the source of the data, the year built, and any additional notes on information relevant to the structure.

B-2. Cost Distance Analysis

A cost distance test was used to ensure the accuracy of hazard layers, particularly inundation extents. The hazards are corrected for “unrealistic inundation” by creating a cost surface related to the depth of the water in order to achieve two goals:

1. We refer to that cost internally as a “depth penalty” whereby low depths of water have high costs associated with the ability of water to flow to the next cell. The process has been used to ensure that if water gets to the point of only being a few cm, it should not naturally flow to the next cell, or it should be decreased so that eventually, the flow is halted by the depth penalty.
2. We use this approach to account for any water that is hydrologically disconnected from a water source. In both cases, these are applied to fluvial, tidal, and surge events. The nature of pluvial events does not make them eligible for this post-processing step due to the lack of water sources.

In application, water levels were calculated using the flood depth layer at a fine resolution (3 m) elevation data. A local water depth maximum was then calculated by assigning the maximum water level value of pixels within a set radius to all pixels within that distance. This process ensures that a water level was calculated for the local water source (e.g. rivers), and for areas adjacent to that source. A new water depth layer was then generated by subtracting the high resolution data from the local water level maximum layer. That layer, along with the water source layer, was used as a friction layer to identify areas that were either hydrologically disconnected, or that were protected from a local elevation barrier. Areas identified by this process were flagged for further review by the research team.